Journal of Computational Physics **162,** 33–81 (2000)
doi:10.1006/jcph.2000.6517, available online at http://www.idealibrary.com on IDEAL®

Entropy Splitting and Numerical Dissipation[1]

H. C. Yee, M. Vinokur, and M. J. Djomehri

NASA Ames Research Center, Moffett Field, California 94035

Received August 3, 1999; revised March 28, 2000

A rigorous stability estimate for arbitrary order of accuracy of spatial central difference schemes for initial boundary value problems of nonlinear symmetrizable systems of hyperbolic conservation laws was established recently by Olsson and Oliger (1994, "Energy and Maximum Norm Estimates for Nonlinear Conservation Laws," RIACS Report, NASA Ames Research Center) and Olsson (1995, *Math. Comput.* **64**, 212) and was applied to the two-dimensional compressible Euler equations for a perfect gas by Gerritsen and Olsson (1996, *J. Comput. Phys.* **129**, 245) and Gerritsen (1996, "Designing an Efficient Solution Strategy for Fluid Flows, Ph.D. Thesis, Stanford). The basic building block in developing the stability estimate is a generalized energy approach based on a special splitting of the flux derivative via a convex entropy function and certain homogeneous properties. Due to some of the unique properties of the compressible Euler equations for a perfect gas, the splitting resulted in the sum of a conservative portion and a non-conservative portion of the flux derivative, hereafter referred to as the "entropy splitting." There are several potentially desirable attributes and side benefits of the entropy splitting for the compressible Euler equations that were not fully explored in Gerritsen and Olsson. This paper has several objectives. The first is to investigate the choice of the arbitrary parameter that determines the amount of splitting and its dependence on the type of physics of current interest to computational fluid dynamics. The second is to investigate in what manner the splitting affects the nonlinear stability of the central schemes for long time integrations of unsteady flows such as in nonlinear aeroacoustics and turbulence dynamics. If numerical dissipation indeed is needed to stabilize the central scheme, can the splitting help minimize the numerical dissipation compared to its un-split cousin? Extensive numerical study on the vortex preservation capability of the splitting in conjunction with central schemes for long time integrations will be presented. The third is to study the effect of the non-conservative proportion of splitting in obtaining the correct shock location for high speed complex shock-turbulence interactions. The fourth is to determine if this method can be extended to other physical equations of state and other evolutionary equation sets. If numerical dissipation

[1] Longer version of this paper was published as a NASA Technical Memorandum 208793, August 1999, NASA Ames Research Center; presented at the 8th International Symposium on CFD, September 5–10, 1999, Bremen, Germany.

0021-9991/00

is needed, the Yee, Sandham, and Djomehri (1999, *J. Comput. Phys.* **150**, 199) numerical dissipation is employed. The Yee *et al.* schemes fit in the Olsson and Oliger framework.

Key Words: entropy variables; symmetrizable nonlinear conservation laws; thermally perfect gas; low dissipation; high order methods; compact schemes; high order central differencings; shock-capturing methods; nonlinear filters; conservative differencing; TVD schemes; positive schemes; ENO schemes.

I. INTRODUCTION

The construction of efficient high order low dissipation numerical methods for nonlinear conservation laws has been the subject of much research recently. For smooth flows, it is well known that the standard high order non-dissipative central schemes generate spurious noise leading to nonlinear instability, especially for long time integration applications such as in aeroacoustics, rotorcraft dynamics, and turbulence physics. On the other hand, central schemes in conjunction with linear numerical dissipations are too diffusive for the physical problems in question. At the same time the majority of the available high order high-resolution shock-capturing schemes are too CPU intensive for practical computations. In spite of their high-resolution capability for rapidly evolving flows and short term time integrations, for long time integrations these schemes often exhibit undesirable amplitude errors for aeroacoustics and turbulence computations. Current focus has been mainly on algorithmic issues in constructing highly accurate methods away from boundaries. Rigorous stability estimates for accurate and appropriate numerical boundary conditions associated with fourth- or higher-order methods are equally important and have been the major stumbling block in the theoretical development of these schemes for nonlinear systems. Most of the existing theory for nonlinear conservation laws and their finite discretizations is concerned with the initial value problem (IVP). Standard practice in computational fluid dynamics (CFD) involving boundary conditions relies on guidelines from theory for linear stability analysis of initial boundary value problems (IBVPs) or IVP theories with the boundary conditions ignored. These linearized stability guidelines are only necessary but not sufficient for nonlinear stability. Spatial nonlinear stability of IBVPs goes hand-in-hand with the appropriate amount of nonlinear numerical dissipation required to stabilize the spatial scheme. The delicate balance of the numerical dissipation for stability without the expense of excessive smearing of the flow physics after long time integrations poses a severe challenge for unsteady flow simulations of this type. Actually, there are two possible sources of stabilizing mechanisms, namely, (a) from the governing equation level and (b) from the numerical scheme level. Employing a nonlinear stable form of the governing equations (more conditioned form of the PDE) in conjunction with the appropriate nonlinear stable scheme for IBVPs is one way of minimizing the use of numerical dissipation.

Until recently it was not known how to derive the proper numerical boundary conditions for a rigorous stability estimate for conventional *spatial high order central difference* schemes for nonlinear hyperbolic IBVPs. Advances by Kreiss and Scherer [1], Strand [2], and Olsson [3] led to the construction of high order boundary difference operators that enabled the design of stable high order central schemes for linear hyperbolic systems. The major tool used to overcome the stumbling block is a generalized energy method. The basic building block in establishing a stable energy estimate for high order spatial central

schemes for nonlinear hyperbolic conservation laws consists of two parts. The first is a special transformation of the conservation laws to an appropriate form for the application of the continuous energy estimate for a stable IBVP of the governing equations. The second is a compatible numerical boundary difference operator for the application of the discrete analogue of the continuous energy estimate for a stable IBVP of the discretized counterparts.

From the governing equation level. The energy method for deriving stability estimates for hyperbolic IBVPs was first applied to the nonlinear scalar case by Gustafsson and Olsson [4]. It was then generalized and extended to nonlinear systems of symmetrizable hyperbolic conservation laws by Olsson and Oliger [5] and Olsson [6, 7], and it was applied to the two-dimensional (2-D) compressible Euler equations for a perfect gas by Gerritsen [8] and Gerritsen and Olsson [9]. The transformation that is used relies on the symmetrizability of the systems of nonlinear hyperbolic conservation laws, the possession of a convex entropy function, and a suitable splitting of the flux derivative vector with certain homogeneous properties. Olsson and Oliger [5] utilized the result of Harten [10] on symmetric forms for systems of conservation laws as the backbone. Convexity of the flux functions is not required.

From the numerical scheme level. The aforementioned building blocks in turn allow one to use a modified form of the energy estimate (or generalized energy estimate) in deriving a compatible set of numerical boundary conditions that are stable for the higher-order central differencing schemes. The compatible boundary difference operator has to satisfy the discrete analogue of the integration-by-parts procedure used in the continuous energy estimate (Strand [2]).

Olsson proved that conservation is possible for second-order central schemes. To obtain a rigorous estimate for higher-order central schemes, one must apply the scheme to the split form of the flux derivative, written in non-conservative form, in terms of the transformed variables. The resulting splitting is hereafter referred to as the entropy splitting of the flux derivative or *entropy splitting* for ease of reference. Here, the entropy splitting should not be confused with the traditional flux vector splittings such as the Steger and Warming splitting [11] or other variants. The traditional flux vector splitting splits the *flux function* into different parts and most often into upwind and downwind portions. However, the entropy splitting splits the *flux derivative* using the properties of the chosen entropy function and the symmetrizability of the conservation laws without reference to any upwinding.

Compressible Navier–Stokes equations. Harten showed that the viscous terms of the compressible Navier–Stokes equations can also be symmetrized. In this case, only symmetry is needed in the derivation of the energy estimate. Due to the parabolic nature of the boundary conditions, the homogeneity properties are not required for the Navier–Stokes equations. For the numerical study involving the compressible Navier–Stokes equations in the present study, we apply the entropy splitting to the inviscid fluxes and the symmetric form of the viscous terms is not used. This is an attempt to examine if entropy splitting of the inviscid flux derivatives alone will provide side benefits over the un-split approach.

Active research in the use of the symmetric form of the governing equations was carried out by Hughes *et al.* [12] and related recent work. Hughes *et al.* utilized only the symmetric idea and employed the physical entropy as one of the entropy variables. Their resulting inviscid flux vector and transformed state vector are not homogeneous in the entropy variables. Unlike the entropy splitting, their transformed equations are in purely

non-conservative form. They have enjoyed improved results over the standard conservation law formulation. Their approach, however, does not allow a rigorous stability estimate for IBVPs for nonlinear hyperbolic conservation laws. In addition, due to their use of the purely non-conservative form, it is not certain that a correct shock speed can be obtained in general.

Entropy splitting and weak solutions. The entropy splitting is not limited to smooth solutions. Olsson and Oliger also extended their result to weak solutions (problems containing discontinuities) that are obtained as pointwise limits of vanishing viscosity solutions. The entropy equality condition for the smooth solution case now becomes an entropy inequality condition. In addition, appropriate numerical dissipation is needed in conjunction with central schemes to pick out the physically relevant solutions if weak solutions are present. Gustafsson and Olsson proposed a scalar filter as numerical dissipation. Gerritsen and Olsson proposed the use of a slightly different nonlinear scalar filter in conjunction with wavelets as a shock detection and grid adaptation. The recently developed high order low-dissipative shock-capturing schemes using characteristic filters of Yee *et al.* [13] fit in the entropy splitting framework. Instead of applying a scalar filter, they supply nonlinear filters based on, locally, the different wave characteristics of the convective flux. For complex shock waves, shear and turbulence interactions, one has better control of the amount of dissipation associated with each wave. For efficiency, Yee *et al.* proposed a combination of narrow grid stencil higher-order compact or non-compact centered non-dissipative classical spatial differencing schemes and low order total variation diminishing (TVD), essentially non-oscillatory (ENO) or weighted ENO (WENO) dissipations as nonlinear characteristic filters with an artificial compression method (ACM) sensor. The ACM sensor is the same as that of Harten [14] but utilized in a slightly different context. As an alternative to the ACM sensor, Sjogreen and Yee [15] utilized non-orthogonal wavelet basis functions as multi-resolution sensors to dynamically determine the amount of nonlinear numerical dissipation to be added at each grid point. The resulting sensor function is also readily applicable for grid adaptation purposes. The multi-resolution wavelet sensor, to some extent, is similar to the one of Gerritsen and Olsson, but is utilized in a different context.

Unlike the hybrid schemes, the higher-order non-dissipative scheme is always activated. The final grid stencil of these schemes is five in each spatial direction if second-order TVD schemes are used as filters and seven if second-order ENO schemes are used as filters for a fourth-order base scheme. There is only a 10% increase in operations count over standard second-order TVD schemes for 2-D direct numerical simulations (DNS). Studies showed that higher accuracy was achieved with fewer grid points when compared with that of standard higher-order TVD, positive, ENO or WENO schemes. See Yee *et al.* [13], Sandham and Yee [16], Sjogreen and Yee [15], Hadjadj *et al.* [17], or references cited therein. Extension of these schemes to curvilinear time varying grids with freestream preservation higher-order metric evaluations is reported in Vinokur and Yee [18]. Table I shows the flow chart of the Yee *et al.* [13] schemes.

Objectives. Motivated by the aforementioned development of entropy splitting, Yee *et al.* [13] proposed, as a followup work, to apply their schemes to the entropy splitting form of the inviscid flux derivatives. This paper is a sequel to [13]. Besides investigating some of the fundamental issues described below, studies will be conducted to determine to what extent the entropy splitting form of the flux derivative can help in minimizing numerical dissipation, or equivalently, in improving nonlinear stability in conjunction with the Yee *et al.* [13] schemes. Our main goal is to explore the possible side benefits of the entropy splitting *without* considering the accompanying stable numerical boundary difference operator as a

TABLE I

Flow Chart of the Efficient Low Dissipative High Order Schemes

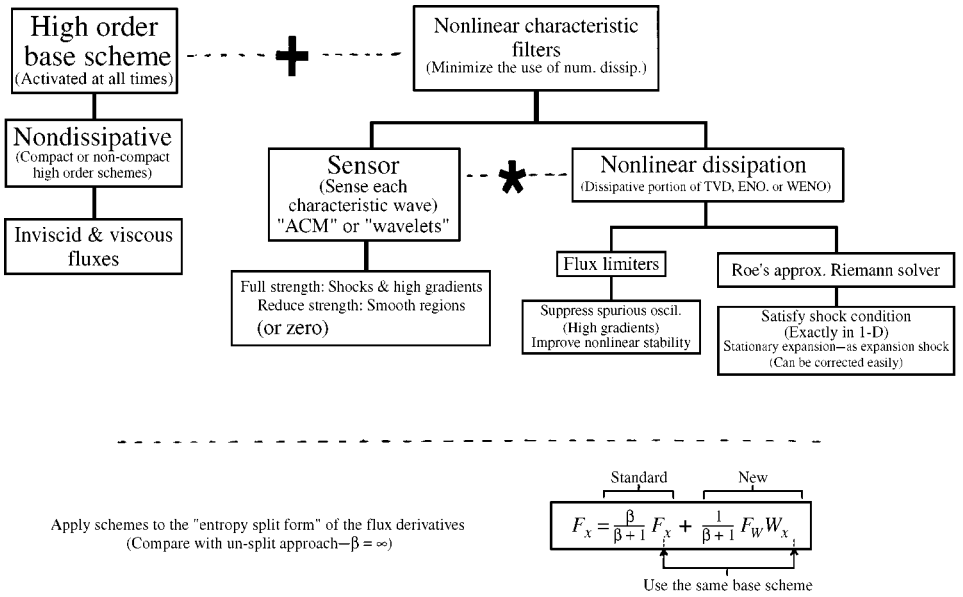

complete package for stability requirements. This is accomplished by choosing numerical examples with periodic boundary conditions, or computational domains whose boundaries are far enough away so as not to affect the mainstream flow activities, and/or by using lower order non-characteristic boundary schemes.

The related fundamental issues to be addressed are that there are several potentially desirable attributes of the entropy splitting for the compressible Euler equations that were not fully explored in Gerritsen and Olsson. First, in regions of smooth flows, additional numerical dissipation might not be required by the entropy splitting in conjunction with non-dissipative spatial central difference schemes. Second, the splitting appears to improve nonlinear stability over the un-split approach employing the same non-dissipative higher-order central schemes even for periodic boundary conditions. Third, the non-conservative portion of the flux derivative seems to have a small effect in obtaining correct shock speeds on the physical problems that Gerritsen and Olsson considered. Fourth, the entropy splitting in conjunction with higher-order central differencing could be a good candidate for nonlinear aeroacoustics, rotorcraft dynamics, and turbulence computations where simplicity, high accuracy, and low numerical dissipation are essential. But most of all, the splitting could possibly be extended to other physical equations of state and other evolutionary equation sets.

Aside from stability considerations, as explained in Harten [10], another potentially desirable attribute in the use of the symmetric form of the governing equations is for the computation of the steady-state solution of the conservation laws. In solving the steady nonlinear conservation laws, the symmetry of the matrix coefficients could possibly enhance the structure of iterative matrices in direct Newton-iteration methods. For time-marching to steady states or time accurate subiteration procedures using implicit methods, the symmetric form in conjunction with the entropy splitting might result in an improved convergence rate over the un-split approach. This will be a subject of future research.

Outline. Section II reviews the entropy splitting and the numerical schemes for the 2-D compressible Euler equations for a perfect gas. The choice of the entropy splitting parameter is discussed in Subsection 2.2. Section III describes the extension of the entropy splitting to other physical equations of states and evolutionary equation sets. Section IV illustrates the performance of the entropy splitting for a variety of unsteady flows and compares the results with those obtained using the un-split conservative approach. The study concentrates only on perfect gases.

In this paper, unless indicated, Euler or Navier–Stokes equations pertain to compressible fluids. High order central difference schemes refer to fourth or higher-order spatial central difference schemes (compact or non-compact methods) without numerical dissipation added. Compatible time discretizations (in terms of stability and accuracy) should be used, but these are not the subject of this paper. The terms "split" and "un-split" mean the application of the same discretization to the "entropy splitting of the inviscid flux derivative" and the standard "inviscid flux derivative in terms of the conservative variables without splitting."

II. ENTROPY SPLITTING FOR A PERFECT GAS

This section reviews the basic building blocks for the entropy splitting for the 2-D compressible Euler equations for a perfect gas in Cartesian coordinates. Formulas for the corresponding 3-D case can be found in Appendix B of Yee *et al.* [19] and in curvilinear moving grids in Section III and in Vinokur and Yee [18]. The mathematical theory is quite involved. Interested readers are referred to references cited. The Yee *et al.* [13] numerical methods used in conjunction with the entropy splitting are also summarized.

2.1. *Summary of Entropy Splitting for a Perfect Gas*

In vector notation the 2-D compressible time-dependent Euler equations in conservation form for an equilibrium real gas can be written, in Cartesian coordinates, as

$$U_t + F_x + G_y = 0, \tag{2.1.1a}$$

where $U_t = \frac{\partial U}{\partial t}$, $F_x = \frac{\partial F}{\partial x}$, and $G_y = \frac{\partial G}{\partial y}$ and the U, F, G, are vectors given by

$$U = \begin{bmatrix} \rho \\ \rho u \\ \rho v \\ e \end{bmatrix}; \qquad F = \begin{bmatrix} \rho u \\ \rho u^2 + p \\ \rho uv \\ eu + pu \end{bmatrix}; \qquad G = \begin{bmatrix} \rho v \\ \rho uv \\ \rho v^2 + p \\ ev + pv \end{bmatrix}. \tag{2.1.1b}$$

The dependent variable U is the vector of conservative variables, and $(\rho, u, v, p)^T$ is the vector of primitive variables. Here ρ is the density, u and v are the velocity components, ρu and ρv are the x- and y-components of the momentum per unit volume, p is the pressure, $e = \rho[\varepsilon + (u^2 + v^2)/2]$ is the total energy per unit volume, and ε is the specific internal energy.

For a thermally perfect gas, the equation of state is

$$p = \rho RT, \tag{2.1.2}$$

where R is the specific gas constant, and T is the temperature with $\varepsilon = \varepsilon(T)$. For constant specific heats (calorically perfect gas)

$$\varepsilon = c_v T, \tag{2.1.3}$$

where c_v is the specific heat at constant volume.

The eigenvalues associated with the flux Jacobian matrices of F and G are $(u, u, u \pm c)$ and $(v, v, v \pm c)$, where c is the sound speed. The two u, u and v, v characteristics are linearly degenerate. Hereafter, we refer to the fields associated with the $u \pm c$ and $v \pm c$ characteristics as the *nonlinear fields* and the fields associated with the u, u and v, v characteristics as the *linear fields*.

Gerritsen and Olsson extended the summation-by-parts idea of Strand, and the entropy splitting of Olsson and Olsson and Oliger to the 2-D Euler equations for an ideal gas in conjunction with high order central schemes. The first step in deriving the entropy splitting for the compressible Euler equations for a perfect gas is to introduce a symmetry transformation from the vector of conservative variables U to a new vector of symmetry variables W, referred to as the "entropy variables." The transformation is chosen so that $F_W = \frac{\partial F}{\partial W}$ and $G_W = \frac{\partial G}{\partial W}$ are symmetric, and $U_W = \frac{\partial U}{\partial W}$ is symmetric and positive definite. A family of symmetry transformations, based on a scalar convex function η, referred to as an "entropy function," derived for the Euler equations for a perfect gas by Harten [10], was employed by Gerritsen and Olsson. It has the form

$$\eta = \rho \xi(\bar{S}). \tag{2.1.4}$$

The function $\xi(\bar{S})$ is an arbitrary but differentiable function of a dimensionless physical entropy

$$\bar{S} = \log(p\rho^{-\gamma}), \tag{2.1.5}$$

where $\bar{S}$ has been non-dimensionalized by c_v. The entropy variables W are then given by $W = \frac{\partial \eta}{\partial U}$. The entropy function η is not to be confused with the "physical entropy" $\bar{S}$ or the entropy variables vector W. The next step is to restrict the transformations to those that allow a special splitting of the flux derivatives. This requires that the entropy variable W is chosen such that $F(U(W))$, $G(U(W))$, and $U(W)$ are homogeneous functions of W of degree β; i.e., there is a constant β such that for all τ

$$U(\tau W) = \tau^\beta U(W), \tag{2.1.6}$$

$$F(\tau W) = \tau^\beta F(W). \tag{2.1.7}$$

The homogeneity property implies that

$$F_W W = \beta F(U(W)) \tag{2.1.8}$$

$$U_W W = \beta U. \tag{2.1.9}$$

Then the splitting of F_x results in

$$F_x = \frac{1}{\beta+1}(F_W W)_x + \frac{1}{\beta+1} F_W W_x = \frac{\beta}{\beta+1} F_x + \frac{1}{\beta+1} F_W W_x, \qquad \beta \neq -1. \tag{2.1.10}$$

A similar splitting can be written for G_y and U_t. Under these conditions one can rigorously establish a bound on the rate of growth of the energy norm in terms of the absolute eigenvalues corresponding to the incoming characteristic variables at the boundary of the domain.

For a perfect gas, the required entropy function is obtained by letting $\xi(\bar{S}) = Ke^{\bar{S}/(\alpha+\gamma)}$, where K and α are constants. The corresponding W can be written as

$$W = [w_1 \quad w_2 \quad w_3 \quad w_4]^T = \frac{p^*}{p}\left[e + \tfrac{\alpha-1}{\gamma-1}p \quad -\rho u \quad -\rho v \quad \rho\right]^T \tag{2.1.11a}$$

and the upper triangular part of the symmetric matrix U_W is

$$U_W = \frac{1}{p^*}\begin{bmatrix} a\rho & a\rho u & a\rho v & \frac{a}{2}\rho(u^2+v^2) - \frac{1}{\gamma-1}p \\ & a\rho u^2 - p & a\rho uv & u\left[\frac{a}{2}\rho(u^2+v^2) - bp\right] \\ & & a\rho v^2 - p & v\left[\frac{a}{2}\rho(u^2+v^2) - bp\right] \\ & & & -\frac{b}{\gamma-1}\frac{p^2}{\rho} - bp(u^2+v^2) + \frac{a}{4}\rho(u^2+v^2)^2 \end{bmatrix}. \tag{2.1.11b}$$

The constants a and b are $a = (1-\alpha-\gamma)/\alpha$ and $b = \gamma/(\gamma-1)$. Here, p^* and p are related through

$$p^* = \chi e^{\frac{\bar{S}}{(\alpha+\gamma)}} = \chi(p\rho^{-\gamma})^{\frac{1}{(\alpha+\gamma)}}, \tag{2.1.11c}$$

with $\chi = -\frac{K}{\beta} < 0$. In the authors' opinion, the simplest choice is to set $K = \beta$. The parameter β is given by

$$\beta = \frac{\alpha+\gamma}{1-\gamma}. \tag{2.1.11d}$$

Using (2.1.1b), (2.1.2), (2.1.3), (2.1.11a), and (2.1.11d), we can show (see Subsection 3.1) that U, F, and G are homogeneous functions of W of degree β. The positive definite condition on U_W (see Subsection 3.1) restricts α to the two ranges $\alpha > 0$ or $\alpha < -\gamma$.

The flux vectors, expressed in the W variables, are given by

$$F(U(W)) = \frac{p}{p^*}\left[-w_2 \quad \tfrac{w_2^2}{w_4} + p^* \quad \tfrac{w_2 w_3}{w_4} \quad -\tfrac{w_2}{w_4}\left(w_1 + \tfrac{\gamma-\alpha}{\gamma-1}p^*\right)\right]^T, \tag{2.1.11e}$$

$$G(U(W)) = \frac{p}{p^*}\left[-w_3 \quad \tfrac{w_2 w_3}{w_4} \quad \tfrac{w_3^2}{w_4} + p^* \quad -\tfrac{w_3}{w_4}\left(w_1 + \tfrac{\gamma-\alpha}{\gamma-1}p^*\right)\right]^T. \tag{2.1.11f}$$

The upper triangular parts of the symmetric matrices $F(U(W))_W$ and $G(U(W))_W$, expressed in the U variables, are given by

$$F_W = \frac{1}{p^*}\begin{bmatrix} a\rho u & a\rho u^2 - p & a\rho uv & u\left[\frac{a}{2}\rho(u^2+v^2) - bp\right] \\ & u(a\rho u^2 - 3p) & v(a\rho u^2 - p) & -b\frac{p^2}{\rho} + \hat{c}pu^2 + \frac{a}{2}\rho(u^2+v^2)u^2 \\ & & & -\frac{1}{2}p(u^2+v^2) \\ & & u(a\rho v^2 - p) & uv\left[\hat{c}p + \frac{a}{2}\rho(u^2+v^2)\right] \\ & & & u\left[b\hat{c}\frac{p^2}{\rho} + \hat{c}p(u^2+v^2)\right. \\ & & & \left. + \frac{a}{4}\rho(u^2+v^2)^2\right] \end{bmatrix}, \tag{2.1.11g}$$

$$G_W = \frac{1}{p^*}\begin{bmatrix} a\rho v & a\rho uv & a\rho v^2 - p & v\left[\frac{a}{2}\rho(u^2+v^2) - bp\right] \\ & v(a\rho u^2 - p) & u(a\rho v^2 - p) & uv\left[\hat{c}p + \frac{a}{2}\rho(u^2+v^2)\right] \\ & & v(a\rho v^2 - 3p) & -b\frac{p^2}{\rho} + \hat{c}pv^2 - \frac{1}{2}p(u^2+v^2) \\ & & & \quad + \frac{a}{2}\rho(u^2+v^2)v^2 \\ & & & v\left[b\hat{c}\frac{p^2}{\rho} + \hat{c}p(u^2+v^2)\right. \\ & & & \quad \left. + \frac{a}{4}\rho(u^2+v^2)^2\right] \end{bmatrix}, \tag{2.1.11h}$$

where $\hat{c} = (1-2\gamma)/(\gamma-1)$.

2.2. *Choice of the Entropy Splitting Parameter*

From the structure of (2.1.10), the entropy splitting divides the flux derivative into a conservative and a non-conservative part. The ratio between the conservative and non-conservative parts depends on the choice of the parameter β. Both Harten [10] and Gerritsen and Olsson introduced the parameter α. In the authors' opinion, the introduction of α is not necessary. However, to adhere to the discussion when referencing their work, we retain the use of α in the perfect gas case. The convexity condition on the entropy function η restricts the value α to two possible ranges; namely, $\alpha > 0$ or $\alpha < -\gamma$ (or equivalently, $\beta < \frac{\gamma}{1-\gamma}$ or $\beta > 0$). Although Gerritsen and Olsson considered the $\alpha < -\gamma$ range which Harten overlooked, they set $\alpha = 1-2\gamma$ ($\beta = 1$) in conjunction with high order central differencing schemes in all of their numerical examples. This choice of α corresponds to the splitting of the flux derivative into equal conservative and non-conservative proportions. They did not give any guidelines or examples of the effect of the choice of α on the quality of the numerical solutions for different flow physics. In addition, all of their examples deal with at most simple shock waves, if present. Wavelets are used as shock detectors and to guide the grid adaptation. Due to the type of problem they addressed and the dense clustering of the grid points near the shocks using very small time steps, it is not certain that correct shock speeds were really obtained with a reasonably practical time step and grid distribution. It is the purpose of this section to discuss the choice of the α parameter value. We discuss $\alpha > 0$ and $\alpha < -\gamma$ separately.

The $\alpha > 0$ (or $\beta < \frac{\gamma}{1-\gamma}$) Case. This is the only case that Harten considered. This corresponds to a negative β which results in a conservative proportion $fr_c = \frac{\beta}{1+\beta} > 1$ and a non-conservative proportion $fr_{nc} = \frac{1}{1+\beta} < 0$. As $\alpha \to 0^+$, $fr_c \to \gamma^-$ and $fr_{nc} \to (1-\gamma)^+$. Here, the superscripts $+$ and $-$ indicate the values approach the limit from above and below, respectively. Thus, it appears that $\alpha > 0$ is "nonstandard" or "nonphysical" in the sense that a larger than 100% of the conservative proportion and a negative non-conservative proportion is used. As $\alpha \to 0^+$, the proportion becomes extremely unphysical. As $\alpha \to \infty$, $fr_c \to 1^+$ and $fr_{nc} \to 0^-$. Therefore as $\alpha \to \infty$, the proportion becomes more physical.

The $\alpha < -\gamma$ (or $\beta > 0$) Case. The $\alpha < -\gamma$ case corresponds to a positive β and consequently, $fr_c < 1$ and $fr_{nc} < 1$. We have the following five situations.

(i) As $\alpha \to -\gamma$, $\beta \to 0^+$, $fr_c \to 0^+$, and $fr_{nc} \to 1^-$.

(ii) For $\alpha = 1 - 2\gamma$, $\beta = 1$, $fr_c = 1/2$, and $fr_{nc} = 1/2$.
(iii) For $1 - 2\gamma < \alpha < -\gamma$, $fr_c < 1/2$ and $fr_{nc} > 1/2$.
(iv) For $\alpha < 1 - 2\gamma$, $fr_c > 1/2$ and $fr_{nc} < 1/2$.
(v) As $\alpha \to -\infty$, $fr_c \to 1^-$ and $fr_{nc} \to 0^+$.

Section IV gives a parameter study of α for three different types of flow physics.

2.3. *Numerical Methods*

The spatial discretizations for weak solutions proposed in [13] consist of two parts, namely, a base scheme and a filter. When numerical dissipations or filters are not used, the scheme consists of only the base scheme. This section discusses the base scheme and Subsection 2.4 discusses the form of the filter (numerical dissipation) for complex shock waves, shear and turbulence interactions. Subsection 2.6 discusses the blending of the Yee *et al.* [13] filters with other filters for the suppression of spurious high frequency oscillations.

2.3.1. Spatial base schemes for the convection terms. Denote $F_{j,k}$ as the discrete approximation of the convection flux F at $(j\Delta x, k\Delta y)$, where Δx and Δy are the grid spacing in the x- and y-directions and j and k are the corresponding spatial indices. Possible non-dissipative high order base schemes for F_x (similarly for G_y) can be of the following two types.

Central differencings (fourth and sixth order).

$$F_x \approx \frac{1}{12\Delta x}(F_{j+2,k} - 8F_{j+1,k} + 8F_{j-1,k} - F_{j-2,k}), \tag{2.3.1}$$

$$F_x \approx \frac{1}{60\Delta x}(F_{j+3,k} - 9F_{j+2,k} + 45F_{j+1,k} - 45F_{j-1,k} + 9F_{j-2,k} - F_{j-3,k}). \tag{2.3.2}$$

Compact central differencings (fourth and sixth order).

$$F_x \approx \frac{1}{\Delta x}\left(A_x^{-1}B_xF\right)_{j,k}, \tag{2.3.3a}$$

where for a fourth-order approximation

$$(A_xF)_{j,k} = \frac{1}{6}(F_{j+1,k} + 4F_{j,k} + F_{j-1,k}), \tag{2.3.3b}$$

$$(B_xF)_{j,k} = \frac{1}{2}(F_{j+1,k} - F_{j-1,k}), \tag{2.3.3c}$$

and for a sixth-order approximation

$$(A_xF)_{j,k} = \frac{1}{5}(F_{j+1,k} + 3F_{j,k} + F_{j-1,k}), \tag{2.3.3d}$$

$$(B_xF)_{j,k} = \frac{1}{60}(F_{j+2,k} + 28F_{j+1,k} - 28F_{j-1,k} - F_{j-2,k}). \tag{2.3.3e}$$

2.3.2. Spatial schemes for viscous terms. For simplicity let V_{xx} be a viscous term in one dimension. The possible high order base schemes for V_{xx} can be

Central differencings (fourth and sixth order).

$$V_{xx} \approx \frac{1}{12\Delta x^2}(V_{j+2} - 16V_{j+1} + 30V_j - 16V_{j-1} + V_{j-2}), \tag{2.3.4}$$

$$V_{xx} \approx \frac{1}{180\Delta x^2}(2V_{j+3} - 27V_{j+2} + 270V_{j+1} - 490V_j + 270V_{j-1} - 27V_{j-2} + 2V_{j-3}). \tag{2.3.5}$$

Compact central differencings (fourth and sixth order).

$$V_{xx} \approx \frac{1}{\Delta x^2}\left(C_x^{-1} D_x V\right)_j, \tag{2.3.6a}$$

where for a fourth-order approximation

$$(C_x V)_j = \frac{1}{12}(V_{j+1} + 10V_j + V_{j-1}), \tag{2.3.6b}$$

$$(D_x V)_j = V_{j+1} - 2V_j + V_{j-1}, \tag{2.3.6c}$$

and for a sixth-order approximation

$$(C_x V)_j = V_{j+1} + a_0 V_j + V_{j-1}, \tag{2.3.6d}$$

$$(D_x V)_j = b_0(V_{j+1} - 2V_j + V_{j-1}) + \frac{c_0}{4}(V_{j+2} - 2V_j + V_{j-2}), \tag{2.3.6e}$$

$$a_0 = 5.5, \tag{2.3.6f}$$

$$b_0 = 4(a_0 - 1)/3, \tag{2.3.6g}$$

$$c_0 = (10 - a_0)/3. \tag{2.3.6h}$$

2.4. *Filters*

In this section we first review the procedure for applying the characteristic filter to multistage Runge–Kutta type and linear multistep method (LMM) types of time discretizations [13]. Examples of explicit LMMs are forward Euler and Adams–Bashforth. Examples of implicit LMMs are backward Euler, trapezoidal rule, and three-point backward differentiation. The one-leg formulation of the LMMs of Dahlquist [20] is also applicable. We then discuss forms of the characteristic filter.

2.4.1. Procedure to apply the filter step. If a multistage time discretization such as the Runge–Kutta method is desired, the spatial differencing base scheme discussed in the previous section is applied at every stage of the Runge–Kutta method. If viscous terms are present, we use the same order and type of base scheme for the viscous terms as for the convection terms.

There are two methods for applying the characteristic filter. Method 1 is to apply the filter at every stage of the Runge–Kutta step. Method 2 is to apply the filter at the end of the full Runge–Kutta step. For inviscid and strong shock interactions, method 1 might be more stable.

If one desires a time discretization that belongs to the class of LMMs, then the filter can be applied as a numerical dissipation vector in conjunction with the base scheme. The filter

in this case is evaluated at U^n for explicit LMMs. For implicit LMMs additional similar filters evaluated at the $n+1$ time level are involved. Alternatively, method 2 can be applied to LMMs as well. In this case, we apply the filter after the completion of the implicit time step. One can minimize flux evaluations by using the one-leg formulation of the LMMs of Dahlquist. The least dissipative (in time) second-order, two-time level one-leg method is the mid-point implicit method. Note that the noniterative linearized form of the midpoint implicit formula reduces to the regular noniterative linearized trapezoidal formula.

For time marching to steady states using implicit LMMs, certain flow physics only require an explicit dissipation term. Also, the implicit operator can be different from the explicit operator. See [21–26] for some efficient conservative linearized implicit forms.

2.4.2. Nonlinear characteristic filters. There are many possible candidates for the filter operator in conjunction with high order base schemes. Here, we propose using filter operators that have similar width of grid stencils as the base scheme for efficiency and ease of numerical boundary treatment. Higher than third-order filter operators are of course applicable, but they are more CPU intensive and require special treatment near boundary points for stability and accuracy. The filter operator usually consists of the product of a sensor and nonlinear dissipations. Two possible sensor are considered: the ACM sensor [13] or the wavelet sensor (Sjogreen and Yee [15]). See Table I for the roadmap. Here we briefly review the ACM sensor and interested readers are referred to [15] for the wavelet sensor.

We use nonlinear dissipation terms in conjunction with the Harten ACM sensor applied to each characteristic wave as the filter vector. In essence, the nonlinear dissipation terms act as second- or third-order ACM-like operators unlike Harten's first-order ACM (Harten [14]). The sensor is used to signal the amount of nonlinear dissipation to be added to the high order non-dissipative scheme, one wave at a time. Thus, the current approach is also different in spirit to the original Harten [27] second-order TVD scheme which uses ACM to sharpen the contact discontinuities. Let the filter vector in the x-direction be of the form

$$\tilde{F}^*_{j+\frac{1}{2},k} = \frac{1}{2} R_{j+\frac{1}{2}} \Phi^*_{j+\frac{1}{2}}. \tag{2.4.1}$$

$\tilde{F}^*_{j+1/2,k}$ is the modified form of the nonlinear dissipation portion of the standard numerical flux. For characteristic based methods, the quantity $R_{j+1/2}$ is the right eigenvector matrix of $\frac{\partial F}{\partial U}$ using, for example, Roe's approximate average state. Note that the eigenvector $R_{j+1/2}$ should not be confused with the R in (2.1.2). We cast the $\tilde{G}^*_{j,k+1/2}$ in the same manner. The elements of $\Phi^*_{j+1/2}$ denoted by $(\phi^l_{j+1/2})^*$ are

$$\left(\phi^l_{j+\frac{1}{2}}\right)^* = \kappa \theta^l_{j+\frac{1}{2}} \phi^l_{j+\frac{1}{2}}. \tag{2.4.2}$$

The $\phi^l_{j+1/2}$ in (2.4.2) are the elements of $\Phi_{j+1/2}$—the dissipative vector of the high-resolution schemes resulting from using a TVD, ENO, or WENO scheme. Hereafter, we refer to (2.4.2) as the ACM filter.

Formulae for $\phi^l_{j+1/2}$ are well known and can be found in the literature. In most of the numerical computations in Section IV, we use the Harten and Yee [25, 26] second-order upwind TVD numerical dissipation. Computations using the symmetric TVD dissipation (Yee [22]) will also be presented. See [13] for details and for a discussion of other possible filters.

The function $\kappa\theta^l_{j+1/2}$ is the key mechanism for achieving high accuracy of the fine scale flow structure as well as shock waves in a stable manner. In other words, the elements of

$\Phi^*_{j+1/2}$ are the same as the nonlinear dissipation term of the TVD, ENO, or WENO scheme with the exception of premultiplying by $\kappa\theta^l_{j+1/2}$. The parameter κ is problem dependent. For smooth flows, κ is used to improve nonlinear stability and can be very small. Different physical problems require a different value of κ because of the large variation in flow properties. The κ value may vary from one characteristic wave to another, and from one region of the flow field to another region with different flow structure. The range of κ for our present numerical experiments is $0.0 \le \kappa \le 0.7$. The function $\theta^l_{j+1/2}$ is the Harten ACM sensor. For a general $2m+1$ points base scheme, Harten recommended

$$\theta^l_{j+\frac{1}{2}} = \max\left(\hat{\theta}^l_{j-m+1}, \ldots, \hat{\theta}^l_{j+m}\right), \tag{2.4.3}$$

$$\hat{\theta}^l_j = \left| \frac{\left|\alpha^l_{j+\frac{1}{2}}\right| - \left|\alpha^l_{j-\frac{1}{2}}\right|}{\left|\alpha^l_{j+\frac{1}{2}}\right| + \left|\alpha^l_{j-\frac{1}{2}}\right|} \right|^p. \tag{2.4.4}$$

The $\alpha^l_{j+1/2}$ are elements of $R^{-1}_{j+1/2}(U_{j+1,k} - U_{j,k})$.

Instead of varying κ for the particular flow problem, one can vary p. For larger p, less numerical dissipation is added. Note that by varying $p \ge 1$ in (2.4.4), one can essentially increase the order of accuracy of the dissipation term. The order of the dissipation depends on the value of p (Bjorn Sjogreen, private communication, 1998). One can switch from $p = 1$ near shock locations to $p > 1$ at smooth regions. For all of the numerical examples, we use $p = 1$ and

$$\theta^l_{j+\frac{1}{2}} = \max\left(\hat{\theta}^l_j, \hat{\theta}^l_{j+1}\right). \tag{2.4.5}$$

The shock-turbulence interaction problems appear to favor this form of $\theta^l_{j+1/2}$. To avoid the tuning of the arbitrary parameter κ and/or p, one can replace $\kappa\theta^l_{j+1/2}$ by a wavelet sensor $\omega^l_{j+1/2}$ (Sjogreen and Yee [15]) which has been shown to give comparable accuracy for the numerical examples in Yee et al. [13].

2.5. *Computer Implementation*

To avoid some conditional statements in the actual computer code and to promote vectorization, several of the functions inside the filter with the potential of dividing by zero are modified. See [13] for details. In particular, the sensor (2.4.4), with $p = 1$, is replaced by

$$\theta^l_j = \frac{\left|\left|\alpha^l_{j+1/2}\right| - \left|\alpha^l_{j-1/2}\right|\right|}{\left|\alpha^l_{j+1/2}\right| + \left|\alpha^l_{j-1/2}\right| + \epsilon}. \tag{2.4.6}$$

In all of the computations, we take $\epsilon = 10^{-7}$. (Actually, ϵ should have the same dimension as $\alpha^l_{j+1/2}$).

2.6. *Blending ACM or Wavelet Filters with Other Filters*

The ACM filter (2.4.2) or wavelet filters might not be sufficient for (a) time-marching to steady state and (b) spurious high frequency oscillations due to insufficient grid resolution and nonlinear instability away from discontinuities, especially for turbulent and large-eddy simulations. This section discusses the blending of other filters with ACM or wavelet filters.

(a) Time-marching to steady state. For time-marching to steady state one usually needs to add fourth-order linear dissipation to a second-order spatial differencing scheme (Beam and Warming [28]). For the present schemes using characteristic filters, in addition to our filters, one might need to add a sixth-order linear dissipation to a fourth-order spatial base scheme and an eighth-order linear dissipation to a sixth-order spatial base scheme in regions away from shocks for stability and convergence. Let L_d be such an additional filter operator. Take the case of a Runge–Kutta time discretization. There are again two ways of incorporating the L_d operator. One way is to incorporate the L_d operator at every stage of the Runge–Kutta method. Another way is to include the L_d operator after the completion of the Runge–Kutta full step. The best way of applying the L_d operator is most likely problem dependent and time integrator dependent. For LMM type of time integrators, L_d is used in conjunction with our filter step as an additional dissipation.

To minimize the amount of dissipation due to L_d in the vicinity of shock waves, there should be a parameter κ_d (different from κ in (2.4.2)) to reduce the amount in the vicinity of shock waves. The L_d operator can be applied to the conservative, primitive, or characteristic variables. The simplest form is to apply L_d to the conservative variables. Alternatively, since all of the work in computing the average states and the characteristic variables is done for the shock-capturing filter operator, one can apply the L_d operator to the characteristic variables. In this case, parameter κ_d can be a vector so that it is more in tune with our characteristic filters using the approximate Riemann solver. For example, one can set $\kappa = 0$ for the linearly degenerate fields and blend a small amount of κ_d to remove spurious noise generated by the lack of ACM or wavelet filters. This blending of the ACM or wavelet filter with the L_d operator can be applied to time-accurate computations as well. When using the wavelet sensor, one can set $(\kappa_d)^l_{j+1/2} = 1 - \omega^l_{j+1/2}$.

(b) Suppression of spurious high frequency oscillations. The ACM filters might not be able to remove spurious high frequency oscillations effectively unless sufficient grid points are used. For the suppression of unphysical high frequency oscillations due to insufficient grid resolution and nonlinear instability away from discontinuities, higher-order spectral-like filters [29–33] might be needed at the locations where the value of the ACM sensor is very small or zero. If spectral-like filters are needed, a proper blending of ACM or wavelet filters with spectral-like filters can be applied. In this case, we can use the same procedures as the time-marching to the steady state except the L_d operator should be replaced with the spectral-like filters (for compact central schemes).

III. EXTENSION TO OTHER EQUATIONS OF STATE AND EQUATION SETS

In this section we discuss the extension of entropy splitting to more general cases. The method originally was developed for the 2-D Euler equations in Cartesian coordinates for a perfect gas. We show here how it can be extended to flow of a gas that is only thermally perfect. For maximum generality, the analysis is presented for arbitrary three-dimensional, time varying grids. A detailed formulation in conjunction with freestream preservation higher-order metric evaluations for the Yee *et al.* schemes [13] can be found in Vinokur and Yee [18]. For compactness, we employ the vector approach of Vinokur [34]. Here the word vector refers to a physical vector such as velocity or momentum, as distinguished from an algebraic *vector* representing a set of variables. For completeness, the Roe Riemann solver for a thermally perfect gas is included. This is motivated by the fact that if the

characteristic type of nonlinear dissipation or filter is desired, Roe's Riemann solver is normally employed. It is noted that both Steger–Warming flux-vector splitting and Roe's approximate Riemann solver have an exact extension for this case. For the readers unfamiliar with the vector approach of Vinokur, the results for the 2-D and 3-D Euler equations in Cartesian coordinates are given in Appendixes A and B of Yee *et al.* [19]. The caloric equation for an ideal diatomic gas is given in Appendix C of [19]. We also examine the possible extensions to a nonequilibrium mixture of species, magnetohydrodynamics, and the artificial compressibility method for incompressible flow.

3.1. *Entropy Splitting for a Thermally Perfect Gas*

In this subsection we derive entropy splitting for a gas that is only thermally perfect, with the internal energy being an arbitrary function of temperature. This law is valid for a dilute gas consisting of a single chemical species and is also a very good approximation for air below the temperature when oxygen starts to dissociate (approximately 2000° K).

The following development describes the derivation leading to a final form of the entropy splitting of the flux derivative for a thermally perfect gas. It has the same form as the perfect gas case, but, the corresponding ranges of the β parameter are different, and W, U_W, and F_W have different expressions. In fact, the derivation of entropy splitting for a perfect gas has to be modified. Certain parameters that are constant for a perfect gas are no longer constant for a thermally perfect gas. In particular, Harten and Gerritsen normalized their entropy S by c_v, which is now a variable for a thermally perfect gas. We therefore normalize our S by the gas constant R. This results in differences in our results from theirs involving the quantity $\gamma - 1$. The positive definite condition (or equivalently, the convexity condition) on U_W again restricts β to be in two possible ranges. As mentioned previously, Harten [10] overlooked one of the more physical ranges, and needlessly introduced a parameter α in his solution. Such a parameter has no analogue for the more general thermally perfect gas case, and only serves to complicate the derivation. Harten also introduced an arbitrary constant K, which he then set equal to a particular value in order to simplify the final expressions. We choose a particular value from the beginning and avoided introducing an unneeded constant.

We repeat the equation of state for a thermally perfect gas (2.1.2)

$$p = \rho R T, \tag{3.1.1}$$

where p, ρ, T, and R are the pressure, density, temperature, and gas constant, respectively. The entropy S and internal energy ϵ are then related to ρ and T through the first and second laws of thermodynamics by

$$d\hat{S} = \frac{d\epsilon}{\hat{T}} - \frac{d\rho}{\rho}, \tag{3.1.2}$$

where we have introduced the normalized variables

$$\hat{S} = \frac{S}{R} \qquad \text{and} \qquad \hat{T} = RT. \tag{3.1.3}$$

Equation (3.1.1) can then be rewritten as

$$p = \rho \hat{T}. \tag{3.1.4}$$

While $\hat{S}$ is dimensionless, $\hat{T}$ has the same dimension as ϵ. It follows from (3.1.2) that $\epsilon = \epsilon(\hat{T})$ only. All real gases satisfy the conditions $\dot{\epsilon} > 0$ and $\ddot{\epsilon} > 0$, where $\dot{\epsilon} = d\epsilon/d\hat{T}$.

Equation (3.1.2) can be integrated to obtain

$$\rho f = e^{-\hat{S}}, \tag{3.1.5}$$

where

$$f(\hat{T}) = \exp\left(-\int \frac{\dot{\epsilon}}{\hat{T}}\, dT\right). \tag{3.1.6}$$

The arbitrary constant in the integral of (3.1.6) can be absorbed in the definition of $\hat{S}$.

Since conservation laws are expressed in terms of of conserved quantities per unit volume, it is convenient to introduce the internal energy per unit volume $\tilde{\epsilon} = \rho\epsilon$. If $\mathbf{u}$ is the fluid velocity vector, then the set of conservative variables U can be represented by the *vector*

$$U = [\rho \quad \mathbf{m} \quad e]^T, \tag{3.1.7}$$

where $\mathbf{m} = \rho\mathbf{u}$ is the momentum vector per unit volume, and $e = \tilde{\epsilon} + \frac{1}{2}\rho\mathbf{u}\cdot\mathbf{u}$ is the total energy per unit volume. Note the algebraic *vector* U has three elements, of which the second element is the physical vector $\mathbf{m}$. The temperature $\hat{T}(U)$ is obtained by solving the equation

$$\epsilon(\hat{T}) = \frac{e}{\rho} - \frac{1}{2}\frac{\mathbf{m}\cdot\mathbf{m}}{\rho^2}. \tag{3.1.8}$$

Equation (3.1.8) has a unique solution since $\dot{\epsilon} > 0$. Let $\mathbf{n}$ be the unit normal vector in a positive direction to a cell surface in a finite-volume grid, or a coordinate surface in a finite-difference grid. If v_n is the normal component of the velocity of a time-varying surface, and $u_n = \mathbf{u}\cdot\mathbf{n}$, one can define the normal relative velocity component $u' = u_n - v_n$. The set of inviscid normal flux components F_n is given by the *vector*

$$F_n = [\rho u' \quad \mathbf{m}u' + p\mathbf{n} \quad eu' + pu_n]^T. \tag{3.1.9}$$

Following Harten [10], we obtain the transformed variable W from

$$W = \frac{\partial\eta}{\partial U}, \tag{3.1.10}$$

where the function $\eta(U)$ is given by

$$\eta = \rho\xi(\hat{S}). \tag{3.1.11}$$

Here again the second element of the algebraic *vector* F_n is a physical vector quantity. $\xi(\hat{S})$ is an arbitrary function of $\hat{S}$, and $\hat{S}$ can be expressed as a function of U using (3.1.5), (3.1.6), and (3.1.8). Using (3.1.2) and (3.1.8), we can express the differential of (3.1.11) as

$$d\eta = \frac{\dot{\xi}}{p}\{[e - 2\tilde{\epsilon} - p(1+\beta)]\, d\rho - \mathbf{m}\cdot d\mathbf{m} + \rho\, de\}, \tag{3.1.12}$$

where $\dot{\xi} = d\xi/d\hat{S}$ and

$$\beta = -\frac{\xi}{\dot{\xi}}. \tag{3.1.13}$$

Note that β is in general a function of $\hat{S}$. We can rewrite (3.1.12) in the form of a matrix multiplication as

$$d\eta = \frac{\dot{\xi}}{p}[e - 2\tilde{\epsilon} - p(1+\beta) \quad -\mathbf{m} \quad \rho] \begin{bmatrix} d\rho \\ d\mathbf{m} \\ de \end{bmatrix}, \tag{3.1.14}$$

where the vector dot product is implied in multiplying the second element of the row *vector* by the second element of the column *vector*. In the rest of the paper, we will use the convention that in forming the product of two matrix elements, a dot product is implied if each element is either a physical vector or a tensor. From (3.1.10) we can express $d\eta$ as $d\eta = W^T dU$. We thus obtain

$$W = [\bar{w} \quad \mathbf{w} \quad \bar{\bar{w}}]^T = \frac{\dot{\xi}}{p}[e - 2\tilde{\epsilon} - p(1+\beta) \quad -\mathbf{m} \quad \rho]^T. \tag{3.1.15}$$

In order to investigate the homogeneity condition, it is useful to introduce the function

$$\mu(W) = \frac{\bar{w}}{\bar{\bar{w}}} - \frac{\mathbf{w}\cdot\mathbf{w}}{2(\bar{\bar{w}})^2} = -\epsilon(\hat{T}) - \hat{T}(1+\beta). \tag{3.1.16}$$

Note that μ involves only thermodynamic variables and is also a homogeneous function of W of degree 0. Since ϵ is in general a nonlinear function of $\hat{T}$, the homogeneity condition can only be satisfied if $\hat{T}$ is a homogeneous function of W of degree 0. In view of (3.1.5) and (3.1.16) this can only be accomplished if

$$\beta(\hat{S}) = \text{constant}. \tag{3.1.17}$$

We can now solve for $\xi(\hat{S})$ from (3.1.13). The sign of $\dot{\xi}$ determines the positive definite condition on U_W; the scale of $\dot{\xi}$ does not affect any numerical calculations. Anticipating the positive definite condition which will be derived below, we find that the simplest solution of (3.1.13) is

$$\xi = \beta e^{-\hat{S}/\beta}, \tag{3.1.18}$$

which then gives

$$\dot{\xi} = -e^{-\hat{S}/\beta}. \tag{3.1.19a}$$

Substituting (3.1.5), this can be expressed as

$$\dot{\xi} = -(\rho f)^{1/\beta}. \tag{3.1.19b}$$

The expression for $\rho(W)$ obtained using (3.1.4), (3.1.7), (3.1.15), and (3.1.19b) is

$$\rho = \frac{\hat{T}^{\beta}}{f(\hat{T})}(-\bar{\bar{w}})^{\beta}. \tag{3.1.20}$$

Therefore ρ is a homogeneous function of W of degree β. From (3.1.15) and the definition of $\mathbf{m}$ it follows that $\mathbf{u}$, u_n, and u' are all homogeneous functions of W of degree 0. We conclude from definitions (3.1.7) and (3.1.9) that the *vectors* U and F_n are both homogeneous functions of W of degree β.

While we cannot obtain an explicit formula for $U(W)$, we can derive an explicit expression for the symmetric matrix U_W as functions of U. The upper triangular part can be written as

$$U_W = \frac{1}{\dot{\xi}}\begin{bmatrix} a\rho & a\rho\mathbf{u} & ae+bp \\ & a\rho\mathbf{u}\mathbf{u} - p\mathbf{I} & \mathbf{u}[ae+(b-1)p] \\ & & \frac{ae^2}{\rho} + p\left(\frac{2be}{\rho} - \mathbf{u}\cdot\mathbf{u}\right) + \frac{bp^2}{\rho}(1+\beta) \end{bmatrix}, \tag{3.1.21a}$$

where

$$a(\hat{T},\beta) = \frac{1}{\dot{\epsilon}+1+\beta} - 1, \tag{3.1.21b}$$

$$b(\hat{T},\beta) = (1+\beta)a + \beta = \frac{-\dot{\epsilon}}{\dot{\epsilon}+1+\beta}, \tag{3.1.21c}$$

and $\mathbf{I}$ is the identity tensor.

Let $A \equiv U_W$ and $\mathbf{u} = q\mathbf{e}$, where $\mathbf{e}$ is a unit vector in the direction of $\mathbf{u}$ and q is the magnitude of $\mathbf{u}$. The positive definite condition for A is determined by the quadratic form $X^T AX$, where the *vector* X has the general form $X = [x_1 \;\; x_2\mathbf{e} \;\; x_3]^T$, and the dot product is implied in a product involving the unit vector $\mathbf{e}$. Since $\mathbf{e}\cdot\mathbf{e}\mathbf{e}\cdot\mathbf{e} = \mathbf{e}\cdot\mathbf{I}\cdot\mathbf{e} = \mathbf{e}\cdot\mathbf{e} = 1$, the quadratic form can be written in terms of ordinary scalar quantities as $X'^T A' X'$, where $X' = [x_1 \;\; x_2 \;\; x_3]^T$, and the upper triangular part of A' becomes

$$A' = \frac{1}{\dot{\xi}}\begin{bmatrix} a\rho & a\rho q & ae+bp \\ & a\rho q^2 - p & q[ae+(b-1)p] \\ & & \frac{ae^2}{\rho} + p\left(\frac{2be}{\rho} - q^2\right) + \frac{bp^2}{\rho}(1+\beta) \end{bmatrix}. \tag{3.1.22a}$$

Therefore the positive definite condition for U_W is obtained by calculating the signs of the leading principal minors of (3.1.22a). Since the elementary operation of subtracting a multiple of one row from another leaves a determinant unchanged, we can reduce (3.1.22a) by a series of elementary operations to the matrix

$$\frac{1}{\dot{\xi}}\begin{bmatrix} a\rho & a\rho q & ae+bp \\ 0 & -p & -pq \\ 0 & 0 & -\frac{bp^2\beta}{\rho a} \end{bmatrix} \tag{3.1.22b}$$

This matrix is positive definite if the leading principal minors are positive. Since $p > 0$ and $\rho > 0$, we obtain the conditions

$$a/\dot{\xi} > 0, \tag{3.1.23a}$$

$$-a/\dot{\xi}^2 > 0, \tag{3.1.23b}$$

and

$$b\beta/\dot{\xi}^3 > 0. \tag{3.1.23c}$$

From (3.1.23a) and (3.1.23b) it follows that $\dot{\xi} < 0$, a condition already satisfied by (3.1.19a). It then follows from (3.1.23c) that $b\beta < 0$, which can be reduced to

$$\frac{1}{\beta} > \frac{-1}{1+\dot{\epsilon}}. \tag{3.1.24}$$

Condition (3.1.24) is satisfied if $\beta > 0$ or $\beta < -(1+\dot{\epsilon})$. It is easy to show that a value of β in these two ranges satisfies $a < 0$, as required by (3.1.23a). Since $\ddot{\epsilon} > 0$, the maximum value of $\dot{\epsilon}$ occurs at $\hat{T}_{max}$. Therefore, for $\beta < 0$,

$$\beta < -[1+\dot{\epsilon}(\hat{T}_{max})]. \tag{3.1.25}$$

A sufficiency condition, independent of the flow problem, is obtained by replacing $\dot{\epsilon}(\hat{T}_{max})$ by $\dot{\epsilon}(\infty)$.

We can also derive an explicit expression for the symmetric flux Jacobian with respect to the transformed variables, $(F_n)_W$, as functions of U. The upper triangular part can be written as

$$(F_n)_W = \frac{1}{\dot{\xi}} \begin{bmatrix} u'a\rho & u'a\rho\mathbf{u} - p\mathbf{n} & u'(ae+bp) - u_n p \\ & u'(a\rho\mathbf{uu} - p\mathbf{I}) - p(\mathbf{un}+\mathbf{nu}) & a_{23} \\ & & a_{33} \end{bmatrix}, \tag{3.1.26a}$$

where

$$a_{23} = \{u'[ae + (b-1)p] - \mathbf{u}_n p\}\mathbf{u} - \frac{p}{\rho}(e+p)\mathbf{n}, \tag{3.1.26b}$$

and

$$a_{33} = u'\left[\frac{ae^2}{\rho} + p\left(\frac{2be}{\rho} - \mathbf{u}\cdot\mathbf{u}\right) + \frac{bp^2}{\rho}(1+\beta)\right] - 2u_n\frac{p}{\rho}(e+p). \tag{3.1.26c}$$

3.2. *Roe Riemann Solver for a Thermally Perfect Gas*

The extension of Roe's approximate Riemann solver to a thermally perfect gas has been given by Abgrall [35] and also Spekreijse and Hagmeijer [36]. (They actually considered the more general case of a mixture of thermally perfect gases, valid for nonequilibrium flow.) We present the results here for arbitrary three-dimensional grids, using our compact vector notation. The Riemann solver is based on properties of the ordinary flux Jacobian matrix $A = \partial F_n/\partial U$. From (3.1.7) and (3.1.9) it follows that we need the pressure differential

$$dp = \chi\, d\rho + \kappa\, d\tilde{\epsilon}, \tag{3.2.1}$$

where

$$\kappa(\hat{T}) = \frac{1}{\dot{\epsilon}} \qquad \text{and} \qquad \chi(\hat{T}) = \hat{T} - \kappa\epsilon. \tag{3.2.2}$$

The matrix A can then be written as

$$A = \begin{bmatrix} -v_n & \mathbf{n} & 0 \\ K_1\mathbf{n} - u_n\mathbf{u} & \mathbf{u}\mathbf{n} - \kappa\mathbf{n}\mathbf{u} + u'\mathbf{I} & \kappa\mathbf{n} \\ (K_1 - H)u_n & H\mathbf{n} - \kappa u_n\mathbf{u} & u' + \kappa u_n \end{bmatrix}, \tag{3.2.3}$$

where $K_1 = \frac{1}{2}\kappa\mathbf{u}\cdot\mathbf{u} + \chi$, $H = h + \frac{1}{2}\mathbf{u}\cdot\mathbf{u}$ is the total enthalpy per unit mass, and $h = \epsilon + \hat{T}$ is the specific enthalpy. The three distinct eigenvalues of A are

$$\lambda^1 = u', \qquad \lambda^2 = u' + c, \qquad \text{and} \qquad \lambda^3 = u' - c, \tag{3.2.4}$$

where the speed of sound c is given by

$$c^2 = \chi + \kappa h. \tag{3.2.5}$$

The multiple eigenvalue λ^1 is associated with those conservative variables whose flux is purely convective. These are ρ and the tangential component of $\mathbf{m}$. In order to construct the corresponding linearly independent eigenvectors associated with the multiple eigenvalue, we span the plane normal to $\mathbf{n}$ by an arbitrary set of two basis vectors $\mathbf{b}_i$ and the set of reciprocal basis vectors $\mathbf{b}^j$, satisfying $\mathbf{b}_i \cdot \mathbf{b}^j = \delta_i^j$, where δ_i^j is the Kronecker delta. It follows that $\mathbf{b}_i \cdot \mathbf{n} = \mathbf{b}^j \cdot \mathbf{n} = 0$. The right eigenvector matrix R can then be written as

$$R = \begin{bmatrix} 1 & 0 & 1 & 1 \\ \mathbf{u} & c\mathbf{b}_i & \mathbf{u} + c\mathbf{n} & \mathbf{u} - c\mathbf{n} \\ K_2 & c\mathbf{b}_i \cdot \mathbf{u} & H + cu_n & H - cu_n \end{bmatrix}, \tag{3.2.6}$$

where $K_2 = \frac{1}{2}\mathbf{u}\cdot\mathbf{u} - \chi/\kappa$.

Among the various approximate Riemann solvers, the most common one uses the Roe average because of its simplicity and its ability to satisfy the jump conditions across discontinuities exactly. In those solvers based on local linearization, the flux at a point separating two states U^L and U^R is based on the eigenvalues and eigenvectors of some average $\bar{A}$. The optimum choice for $\bar{A}$ is one satisfying

$$\Delta F_n = \bar{A}\,\Delta U, \tag{3.2.7}$$

where $\Delta(\cdot) = (\cdot)^R - (\cdot)^L$. This choice of $\bar{A}$ captures discontinuities exactly. One way of obtaining $\bar{A}$ is to seek an average state $\bar{U}$, which is a function of U^L and U^R, such that

$$\bar{A} = A(\bar{U}). \tag{3.2.8}$$

Such a state is known as a Roe-averaged state. One can easily show that

$$\bar{\mathbf{u}} = \alpha\mathbf{u}^L + (1-\alpha)\mathbf{u}^R \tag{3.2.9}$$

and

$$\bar{H} = \alpha H^L + (1-\alpha) H^R, \tag{3.2.10}$$

where

$$\alpha = \frac{1}{1+\sqrt{\rho^R/\rho^L}}. \tag{3.2.11}$$

From the definition of H one then obtains

$$\bar{h} = \bar{H} - \frac{1}{2}\bar{\mathbf{u}}\cdot\bar{\mathbf{u}}. \tag{3.2.12}$$

The discrete form of (3.2.1) yields the relation

$$\bar{\chi}\,\Delta\rho + \bar{\kappa}\,\Delta\tilde{\epsilon} = \Delta p. \tag{3.2.13}$$

The Roe-averaged sound speed is given by (3.2.5) as

$$\bar{c}^2 = \bar{\chi} + \bar{\kappa}\bar{h}. \tag{3.2.14}$$

Equation (3.2.13) provides only one relation to determine $\bar{\chi}$ and $\bar{\kappa}$. Since χ and κ are functions of $\hat{T}$ only, the simplest assumption is that $\bar{\chi}$ and $\bar{\kappa}$ depend only on $\hat{T}^R$ and $\hat{T}^L$. Eliminating p, using (3.1.4), we rewrite (3.2.13) as

$$\bar{\chi}(\rho^R - \rho^L) + \bar{\kappa}(\rho^R\epsilon^R - \rho^L\epsilon^L) = \rho^R\hat{T}^R - \rho^L\hat{T}^L. \tag{3.2.15}$$

Equating the coefficients of ρ^R and ρ^L on the two sides of (3.2.15) we obtain the relations

$$\bar{\kappa} = \frac{\Delta\hat{T}}{\Delta\epsilon} \tag{3.1.16a}$$

and

$$\bar{\chi} = \frac{\epsilon^R\hat{T}^L - \epsilon^L\hat{T}^R}{\Delta\epsilon}. \tag{3.1.16b}$$

Equations (3.2.16a), (3.2.16b) are replaced by (3.2.2) when $\Delta\epsilon \to 0$. An important quantity in the approximate Riemann solver is the column *vector* $R^{-1}\Delta U$. Its components are the jumps in the characteristic variables. It is given by

$$R^{-1}\Delta U = \begin{bmatrix} \Delta\rho - \Delta p/\bar{c}^2 \\ \bar{\rho}\mathbf{b}^j\cdot\Delta\mathbf{u}/\bar{c} \\ \frac{1}{2}(\Delta p/\bar{c}^2 + \bar{\rho}\mathbf{n}\cdot\Delta\mathbf{u}/\bar{c}) \\ \frac{1}{2}(\Delta p/\bar{c}^2 - \bar{\rho}\mathbf{n}\cdot\Delta\mathbf{u}/\bar{c}) \end{bmatrix} \tag{3.2.17}$$

where

$$\bar{\rho} = \sqrt{\rho^R\rho^L}. \tag{3.2.18}$$

3.3. *Entropy Splitting for Other Equation Sets*

In this subsection we examine the possibility of applying entropy splitting to other equation sets. We first consider nonequilibrium flow, consisting of a mixture of different species, each obeying a thermally perfect gas law. The motivation is again the fact that this case can also be treated exactly with Steger–Warming flux-vector splitting and Roe's approximate Riemann solver. We next consider the equations of magnetohydrodynamics, since there is much current interest in their solution. Finally, we investigate the artificial compressibility method applied to the solution of the incompressible equations.

3.3.1. Nonequilibrium flow. In nonequilibrium flow, we consider a mixture of species, each obeying a thermally perfect gas law. The conservation law now takes the form

$$U_t + \nabla \cdot \mathbf{F} = \mathcal{S}, \tag{3.3.1}$$

where $\mathcal{S}$ is a *vector* consisting of source terms for each species. The equation of state for species i is

$$p^i = \rho^i R^i T, \tag{3.3.2}$$

where p^i, ρ^i, and R^i are the pressure, density, and gas constant for species i, respectively, and T is the temperature of the mixture, assumed to be in thermal equilibrium. If there are ns species in the mixture, the index i takes on values from 1 to ns. The entropy S^i and internal energy ϵ^i are then related to ρ^i and T by

$$d\hat{S}^i = \frac{d\epsilon^i}{R^i T} - \frac{d\rho^i}{\rho^i}, \tag{3.3.3}$$

where we have introduced the normalized variable

$$\hat{S}^i = \frac{S^i}{R^i}. \tag{3.3.4}$$

Note that we have not introduced a normalized $\hat{T}$, since the R^i are different for each species. It again follows from (3.3.3) that $\epsilon^i = \epsilon^i(T)$ only. All real species satisfy the conditions $\dot{\epsilon}^i > 0$ and $\ddot{\epsilon}^i > 0$, where $\dot{\epsilon}^i = d\epsilon^i/dT$. Equation (3.3.3) can be integrated to obtain

$$\rho^i f^i = e^{-\hat{S}^i}, \tag{3.3.5}$$

where

$$f^i(T) = \exp\left(-\int \frac{\dot{\epsilon}^i}{R^i T}\, dT\right). \tag{3.3.6}$$

The arbitrary constant in the integral of (3.3.6) can be absorbed in the definition of $\hat{S}^i$.

We can now define the density of the mixture, ρ, as

$$\rho = \sum_i \rho^i, \tag{3.3.7}$$

the pressure p as

$$p = \sum_i p^i = \rho R T, \tag{3.3.8}$$

where

$$\rho R = \sum_i \rho^i R^i, \tag{3.3.9}$$

and the entropy per unit volume, ρS, as

$$\rho S = \sum_i \rho^i S^i. \tag{3.3.10a}$$

Using (3.3.4), the last equation can be written as

$$\rho R \hat{S} = \sum_i \rho^i R^i \hat{S}^i, \tag{3.3.10b}$$

where

$$\hat{S} = \frac{S}{R}. \tag{3.3.11}$$

Note that since R is no longer a constant, $\hat{S}$ is not proportional to S. Finally, we define the internal energy of the mixture per unit volume as

$$\tilde{\epsilon} = \rho \epsilon = \sum_i \rho^i \epsilon^i. \tag{3.3.12}$$

The set of conservative variables U can be represented by the *vector*

$$U = [\mathcal{R} \quad \mathbf{m} \quad e]^T, \tag{3.3.13a}$$

where the *vector* $\mathcal{R}$ is defined as

$$\mathcal{R} = (\rho^1 \quad \rho^2 \quad \dots \quad \rho^{ns}). \tag{3.3.13b}$$

The temperature $T(U)$ is obtained by solving implicitly the equation

$$\sum_i \rho^i \epsilon^i(T) = e - \frac{1}{2} \frac{\mathbf{m} \cdot \mathbf{m}}{\rho}, \tag{3.3.14}$$

where ρ is given by (3.3.7). Equation (3.3.14) has a unique solution since $\rho^i > 0$ and $\dot{\epsilon}^i > 0$. The set of inviscid normal flux components F_n is given by the *vector*

$$F_n = [\mathcal{R}u' \quad \mathbf{m}u' + p\mathbf{n} \quad eu' + pu_n]^T. \tag{3.3.15}$$

The procedure to obtain the transformed variable W follows that of Subsection 3.1. Equations (3.1.10)–(3.1.13), and (3.1.17)–(3.1.19a) in that subsection are still valid. With the aid of (3.3.3), (3.3.7), (3.3.9), (3.3.10b), and (3.3.14) we obtain

$$W = [\mathcal{W} \quad \mathbf{w} \quad \bar{\bar{w}}]^T, \tag{3.3.16a}$$

where

$$\mathcal{W} = (w^1 \quad w^2 \quad \cdots \quad w^{ns}), \tag{3.3.16b}$$

$$w^i = \frac{\dot{\xi}}{RT}\left[-R^i T(1+\hat{S}-\hat{S}^i) - \beta RT - \epsilon^i + \frac{1}{2}\frac{\mathbf{m}\cdot\mathbf{m}}{\rho^2}\right], \qquad i = 1, \ldots, ns, \tag{3.3.16c}$$

$$\mathbf{w} = -\frac{\dot{\xi}\mathbf{m}}{\rho RT}, \tag{3.3.16d}$$

and

$$\bar{\bar{w}} = \frac{\dot{\xi}}{RT}. \tag{3.3.16e}$$

It is again useful to define a set of functions of W that are homogeneous of degree 0, involving only thermodynamic variables, as

$$\mu^i(W) = \frac{w^i}{\bar{\bar{w}}} - \frac{\mathbf{w}\cdot\mathbf{w}}{2(\bar{\bar{w}})^2} = -R^i T(1+\hat{S}-\hat{S}^i) - \beta RT - \epsilon^i, \qquad i = 1, \ldots, ns. \tag{3.3.17}$$

Equations (3.3.16e) and (3.1.19a) can be combined to yield

$$(-\bar{\bar{w}})^\beta (RT)^\beta = e^{-\hat{S}}. \tag{3.3.18}$$

In order to prove homogeneity, we let

$$\rho^i = a^i(-\bar{\bar{w}})^\beta. \tag{3.3.19}$$

Substituting (3.3.5), (3.3.18), and (3.3.19) into (3.3.17), we obtain

$$\frac{\mu^i + \epsilon^i}{R^i T} + \frac{\beta R}{R^i} + 1 - \beta \ln(RT) + \ln(a^i f^i) = 0. \tag{3.3.20}$$

Combining (3.3.4), (3.3.9), and (3.3.10b) to eliminate ρ^i, yields

$$R = \frac{\sum_i a^i R^i}{\sum_i a^i}. \tag{3.3.21}$$

Substituting (3.3.5), (3.3.18), and (3.3.19) into (3.3.10b), we obtain

$$\beta \ln(RT) = \frac{\sum_i a^i R^i \ln(a^i f^i)}{\sum_i a^i R^i}. \tag{3.3.22}$$

Equation (3.3.20), (3.3.21), and (3.3.22) comprise a set of coupled nonlinear equations for R, T, and a^i as functions of μ^i. Since the μ^i are homogeneous functions of W of degree 0, it follows that R, T, and a^i are all homogeneous functions of W of degree 0. It is then easy to show that U and F_n are homogeneous functions of W of degree β.

In order to obtain an expression for U_W, we can combine the differentials of (3.3.5), (3.3.17), and (3.3.18) to express $d\rho^i$ as a linear combination of dw^i, $d\mathbf{w}$, $d\bar{\bar{w}}$, dR, and dT. From the differentials of (3.3.4), (3.3.5), (3.3.10b), and (3.3.18) we find that dT equals a

linear combination of $d\overline{\overline{w}}$, dR, and *all* the $d\rho^i$. By eliminating $d\rho$ from the differentials of (3.3.4) and (3.3.5) we see that dR is also equal to a linear combination of *all* the $d\rho^i$. Therefore, obtaining U_W requires inverting a dense linear system. It would thus be difficult to establish the positive definite condition. Therefore the extension of the method to nonequilibrium flow is not practically feasible. If the homogeneity condition is not required, then one can use symmetry variables based on the physical entropy, as was shown by Chalot *et al.* [37].

3.3.2. Magnetohydrodynamics. The set of conservative variables U for magnetohydrodynamics is represented by the *vector*

$$U = [\rho \quad \mathbf{m} \quad e \quad \mathbf{B}]^T, \tag{3.3.23a}$$

where $\mathbf{B}$ is the magnetic field vector, and

$$e = \rho\epsilon(T) + \frac{1}{2}\frac{\mathbf{m}\cdot\mathbf{m}}{\rho} + \frac{1}{2}\mathbf{B}\cdot\mathbf{B}. \tag{3.3.23b}$$

The set of inviscid normal flux components F_n is given by the *vector*

$$F_n = \begin{bmatrix} \rho u' \\ \rho u'\mathbf{u} + \mathbf{n}\left(p + \frac{1}{2}\mathbf{B}\cdot\mathbf{B}\right) - B_n\mathbf{B} \\ eu' + \left(p + \frac{1}{2}\mathbf{B}\cdot\mathbf{B}\right)u_n - B_n(\mathbf{u}\cdot\mathbf{B}) \\ u_n\mathbf{B} - B_n\mathbf{u} \end{bmatrix}, \tag{3.3.24}$$

where $B_n = \mathbf{B}\cdot\mathbf{n}$.

Equation (3.3.23a) shows that $\mathbf{B}$ is an element of U, while (3.3.23b) shows that $\frac{1}{2}\mathbf{B}\cdot\mathbf{B}$ is a term in e, which is also an element of U. It follows that both $\mathbf{B}$ and e cannot have the same degree of homogeneity, and therefore U cannot be a homogeneous function. This result is not surprising, since the magnetic field vector is not a true conservative variable and is not expected to behave the same way as the physical conservative variables.

3.3.3. Artificial compressibility method for incompressible flow. For the artificial compressibility method for incompressible flows, the set of conservative variables U for this case is given by

$$U = [p \quad \mathbf{u}]^T, \tag{3.3.25}$$

while the set of inviscid normal flux components F_n is given by

$$F_n = [\sigma u' \quad u'\mathbf{u} + p\mathbf{n}]^T, \tag{3.3.26}$$

where σ is the artificial compressibility. Since the second element of U is $\mathbf{u}$, while one of the terms in the second element of F_n is $\mathbf{uu}\cdot\mathbf{n}$ it follows that U and F_n cannot have the same degree of homogeneity. This is also not surprising, since p is not a true conservative variable. In the compressible case, the velocity has homogeneity of degree 0, and it is the density that is homogeneous of degree β. When the density is no longer a variable, the homogeneity property disappears.

IV. NUMERICAL EXAMPLES

The numerical experiments will be limited to a perfect gas. Three test cases are considered. The first is inviscid and the last two are compressible mixing layer computations. These test cases were also considered in [13]. The three test cases are: (1) a horizontally convecting vortex, (2) a vortex pairing in a time-developing mixing layer with shock waves formed around the vortices, and (3) a shock wave impinging on a spatially evolving mixing layer where the evolving vortices must pass through a shock wave, which in turn is deformed by the vortex passage. For the two mixing layer computations, the study will be limited to the choice of the β that determines the amount of splitting in obtaining the same shock location as the un-split approach. For the Navier–Stokes computations involving entropy splitting, the splitting is applied to the inviscid flux terms, and the symmetric form of the viscous flux is not used (see Section I).

In all of the computations the classical fourth-order Runge–Kutta time discretization is employed. For the purposes of this paper we concentrate on the non-compact central schemes (2.3.1) and (2.3.2) with the same order of accuracy and type of base scheme for the convection and viscous terms (if viscosities are present). Compact schemes (2.3.3) are also applicable, but require nearly twice the CPU time that the non-compact central schemes require for 2-D compressible mixing layer computations and will not be addressed in this paper.

If numerical dissipation is added, the filters (2.4.2), (2.4.5), and (2.4.6) are used at the end of the full Runge–Kutta time step. Roe's average states [38] are used in (2.4.1). For most of the computations, the Harten and Yee (see [21–26]) second-order upwind TVD dissipation for $\phi^l_{j+1/2}$ in (2.4.2) is used. These will be notated as ACM with the following numbers indicating the order of the base scheme for the convection and viscous terms. For example, ACM44 means the use of fourth-order central as the base scheme for both the convection and viscous terms. In order not to introduce additional notation, inviscid flow simulations are designated by the same notation, with the viscous terms not activated. Computations using symmetric TVD dissipation (Yee [22, limiter (2.7b)]) are indicated by adding the letter **S**, as in ACM44**S**. Computations using entropy splitting are indicated by adding the letters ENT at the end as in ACM44-ENT. To examine the performance of the entropy splitting schemes where shock waves are absent, the computations also employ only the non-dissipative central base schemes (without the ACM filters) designated as CEN22, CEN44, and CEN66 for second, fourth, and sixth order, respectively.

The inviscid case uses a uniform Cartesian grid. The two compressible mixing layer test cases use a uniform Cartesian grid in the x-direction and a mildly stretched Cartesian grid in the y-direction. In order to assess the true performance of the algorithm, no attempt is made to enhance the resolution using appropriate adaptive grid procedures. The code used for the Yee *et al.* [13] study is employed for the present study. For non-periodic boundary conditions (BCs), the code reduces to lower order central base schemes near the boundary points. For the current study, we employ the same numerical BCs treatment in order to have a one-to-one comparison with the results obtained in [13]. Appropriate stable boundary difference operators developed by Strand should be used but are not yet implemented for the present study. The global accuracy of the scheme related to intermediate BC treatment for the multi-stage Runge–Kutta method (Carpenter *et al.* [39]) is not addressed here. Except for the vortex convection problem, all computations impose intermediate BC

updates. Special treatment of the temporally (Carpenter *et al.*) and spatially dependent physical BCs related to the Runge–Kutta method is not considered for the two compressible mixing layer cases and such treatment is beyond the scope of this paper. Nonreflecting BCs or characteristic inflow and outflow boundary treatments are also not implemented. As indicated in the objective section, we explore the possible side benefits of the entropy splitting without considering the accompanying stable numerical boundary difference operator as a complete package for stability requirements. The three numerical examples were chosen to consist of periodic BCs, or computational domains whose boundaries are far enough away so as to not affect the mainstream flow activities. For the non-periodic cases, lower order non-characteristic boundary schemes are used. Evaluation of the performance of these schemes for the two compressible mixing layer test cases should take the above assumption into consideration.

4.1. *Isentropic Vortex Evolution*

The first test case is the evolution of a 2-D inviscid isentropic vortex in a freestream with periodic BCs in both spatial directions. The freestream flow velocity, u_∞ and v_∞, pressure, p_∞, and density, ρ_∞ are $(u_\infty, v_\infty) = (1, 0)$ and $p_\infty = \rho_\infty = 1$. An isentropic vortex with no perturbation in entropy ($\delta S = 0$) is added to the freestream flow field as initial conditions. The perturbation values are given by

$$(\delta u, \delta v) = \frac{\hat{\beta}}{2\pi} e^{\frac{1-r^2}{2}} (-\bar{y}, \bar{x}), \tag{4.1.1}$$

$$\delta T = -\frac{(\gamma - 1)\hat{\beta}^2}{8\gamma\pi^2} e^{1-r^2}, \tag{4.1.2}$$

where $\hat{\beta}$ is the vortex strength and $\gamma = 1.4$. Note that the vortex strength $\hat{\beta}$ should not be confused with the β in Subsection 2.1.2. Here $T = \frac{p}{\rho}$, $T_\infty = 1.0$, $(\bar{x}, \bar{y}) = (x - x_{v_0}, y - y_{v_0})$, where x_{v_0} and y_{v_0} are the initial coordinates of the center of the vortex, and $r^2 = \bar{x}^2 + \bar{y}^2$. The entire flow field is required to be isentropic. Thus, for a perfect gas, $p/\rho^\gamma = 1$.

From the relations, $u = u_\infty + \delta u$, $v = v_\infty + \delta v$, $T = T_\infty + \delta T$, and the isentropic relation, the resulting initial state for the conservative variables is given by

$$\rho = T^{\frac{1}{\gamma-1}} = (T_\infty + \delta T)^{\frac{1}{\gamma-1}} = \left[1 - \frac{(\gamma - 1)\hat{\beta}^2}{8\gamma\pi} e^{1-r^2}\right]^{\frac{1}{\gamma-1}} \tag{4.1.3}$$

$$\rho u = \rho(u_\infty + \delta u) = \rho\left[1 - \frac{\hat{\beta}}{2\pi} e^{\frac{1-r^2}{2}} \bar{y}\right] \tag{4.1.4}$$

$$\rho v = \rho(v_\infty + \delta v) = \rho \frac{\hat{\beta}}{2\pi} e^{\frac{1-r^2}{2}} \bar{x} \tag{4.1.5}$$

$$p = \rho^\gamma \tag{4.1.6}$$

$$e = \frac{p}{\gamma - 1} + \frac{1}{2}\rho(u^2 + v^2). \tag{4.1.7}$$

Note that there are misprints for the corresponding Eqs. (4.1.4) and (4.1.5) in [13] (Eqs. (3.4) and (3.5) in [13]).

The exact solution with given initial states is just a passive convection of the vortex with the freestream velocity and thus provides a good measure of the accuracy of the schemes for smooth solutions of the nonlinear Euler equations. The vortex strength $\hat{\beta} = 5$ is fixed for all runs. Let k be the order of the central scheme; then the initial vortex covers a domain $0 \le x \le 10 + 0.125k$ and $-5 \le y \le 5$ and its center is placed at $(x_{v_0}, y_{v_0}) = (5, 0)$. A uniform grid spacing of $\Delta x = 0.125$ and $\Delta y = 10/(79 + k)$ is used. Although the actual grid size is 80×79, regardless of the order of the scheme, the grid size including ghost cells to accommodate the periodic BCs is $(80 + k) \times (79 + k)$. The reason for using an odd number of grid points in the y-direction is due to the compressible mixing layer structure of the code to accommodate fluctuations added to the inflow. The vortex is convected to the right by the mean flow velocity. Since there are no shock waves or steep gradient regions for this flow, the filter is used only to stabilize the nonlinear governing equations. For this reason, the filter coefficient κ (2.4.2), if needed, should be kept very small. We use $0.001 \le \kappa \le 0.07$ for the computations. Due to the isentropic flow property, one can set p^* (2.1.11c) to be a constant. $p^* = 1$ is used for this test case.

Density profiles at the centerline, $y = 0$, cutting through the center of the initial vortex are used for comparing the various schemes. Due to the time and spatial discretization numerical errors, the vortex, after long time integrations, can drift away from the centerline. The amount of drift depends on the scheme, grid size, and the time step. If the computed vortex drifts away from the centerline but still preserves the vortex shape and strength, the centerline, $y = 0$, density profiles do not convey the full information and can be misleading. We complement the comparison with snap shots of density contours at different times up to 110 spatial periods. Here, one period is defined as the length of the periodic computational domain. The time required for one spatial period is $t = 10$. In all of the computations $\delta = 0.1$, where δ is defined by (2.26a) of [13]. The limiter used is that given by Eqs. (2.25f) of [13]. Here, δ is the entropy satisfying parameter of Harten and Hyman [40] for TVD schemes. As recommended by Carpenter *et al.*, no intermediate BC update is imposed to improve the time accuracy of the multistage Runge–Kutta methods. The computations using intermediate BC updates do not have a drastic effect, but tend to diverge a little earlier than the case where there are no intermediate BC updates.

We present results for sixth-order schemes. (Comparisons with second- and fourth-order results are made in the following discussions.) Centerline distributions for CEN66, CEN66-ENT, ACM66, ACM66-ENT, and ACM66**S**-ENT are shown in Figs. 4.1.1–4.1.7. Snapshots of selected density contours for these schemes are shown in Figs. 4.1.8–4.1.12. The performance of the central schemes (with or without ACM) using entropy splitting and their un-split cousins is evaluated based primarily on vortex preservation capability after long time integrations of up to 130 periods ($t = 1300$). The discussion of numerical results is divided into the following:

(a) Effect of the order of accuracy of the base scheme ($\Delta t = 0.04$). We ran some computations with second- and fourth-order accurate base schemes for $\Delta t = 0.04$ (not shown) and compared them with the sixth-order results. CEN22 diverged after 3.5 periods, CEN44 diverged after 6.8 periods, and CEN66 diverged after 5.17 periods. With no dissipation, the more accurate CEN66 computations had nonlinear instability which caused it to diverge slightly earlier than the CEN44 case. Even so, the CEN66 density distribution was very accurate up to 5 periods, as seen from Fig. 4.1.1c. It did show oscillations at period 5, indicating incipient instability at period 5.17.

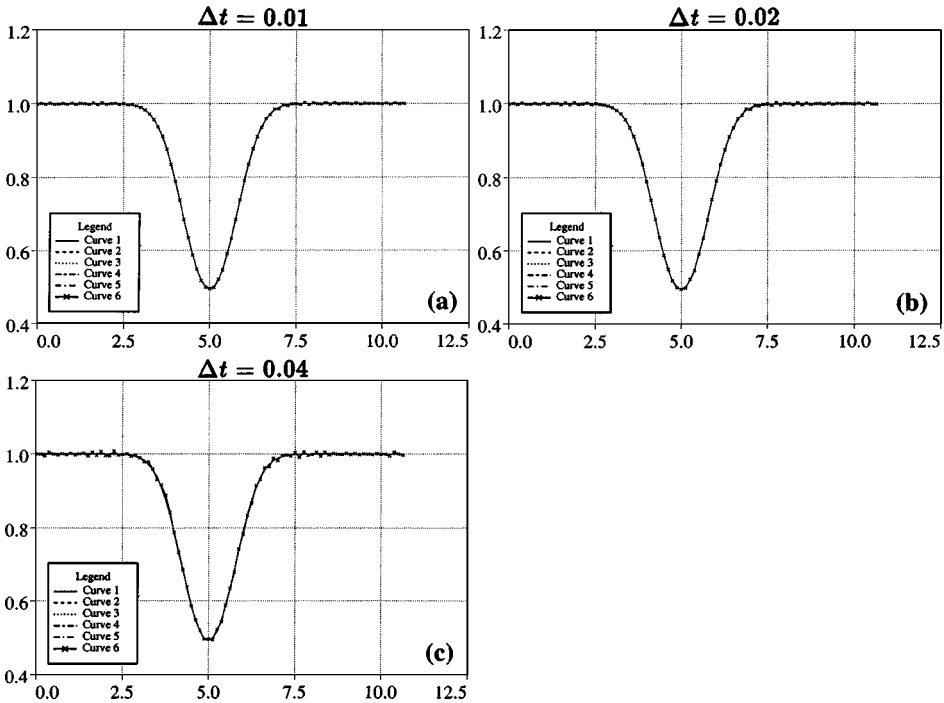

FIG. 4.1.1. Convecting vortex: Comparison of CEN66 with the exact solution (solid line), illustrated by density profiles at the centerline $y = 0$, at $t = 10$, 20, 30, 40, 50 (curves 2–6) for $\Delta t = 0.01$, 0.02, 0.04, on a 80×79 grid.

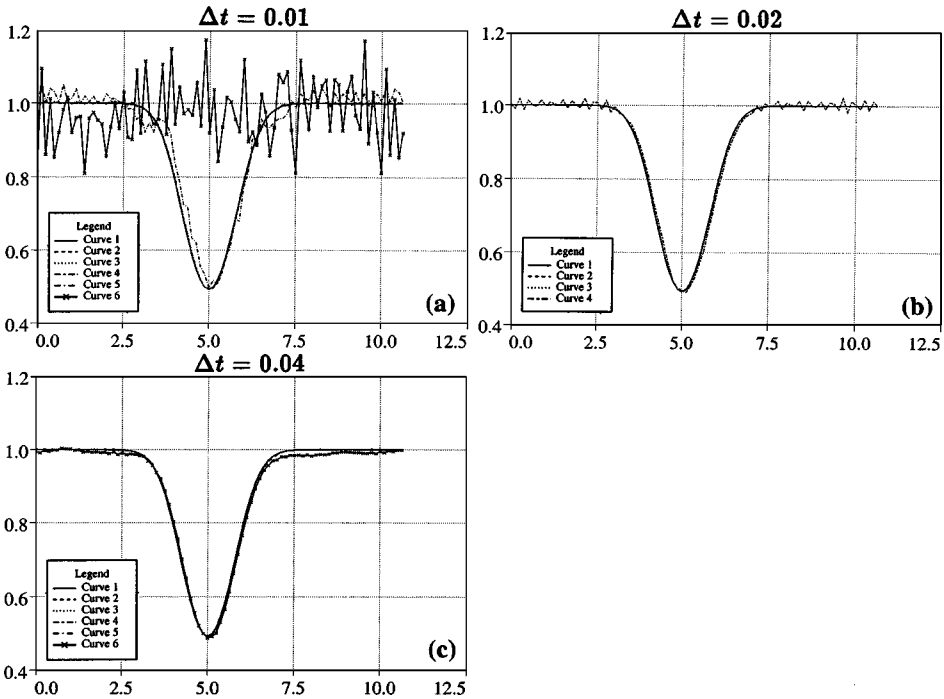

FIG. 4.1.2. Convecting vortex: Comparison of CEN66-ENT with the exact solution (solid line), illustrated by density profiles at the centerline $y = 0$, at $t = 100$, 200, 300, 400, 500 (curves 2–6) for $\Delta t = 0.01$, at $t = 100$, 200, 300 (curves 2–4) for $\Delta t = 0.02$, and at $t = 30$, 50, 100, 150, 160 (curves 2–6) for $\Delta t = 0.04$ on a 80×79 grid.

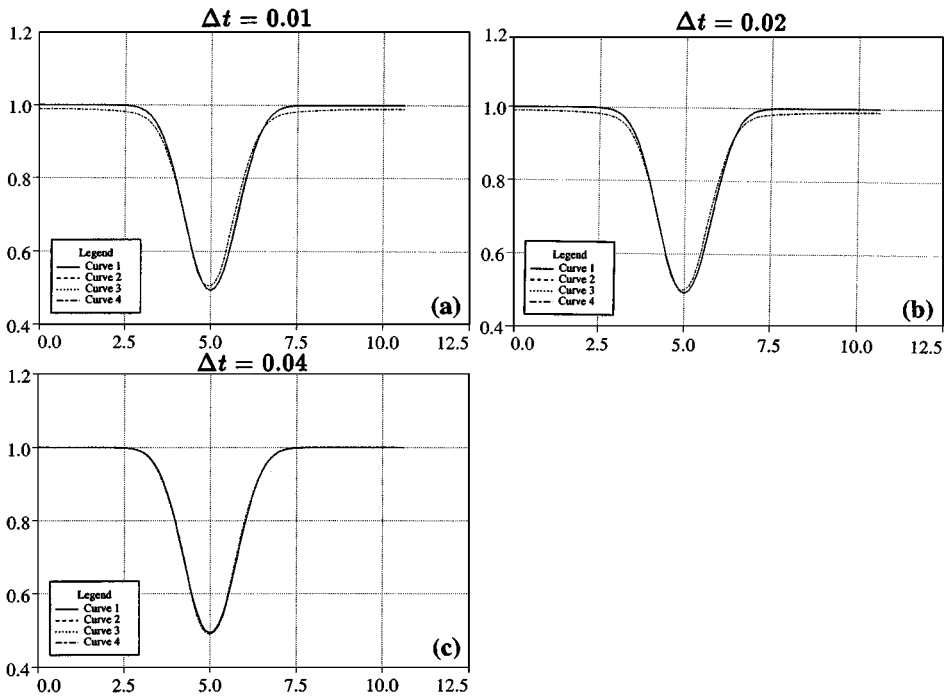

FIG. 4.1.3. Convecting vortex: Comparison of ACM66 with the exact solution (solid line), illustrated by density profiles at the centerline $y = 0$, at $t = 100, 200, 300$ (curves 2–4) for $\Delta t = 0.01, 0.02, 0.04$, $\kappa = 0.06$ on a 80×79 grid.

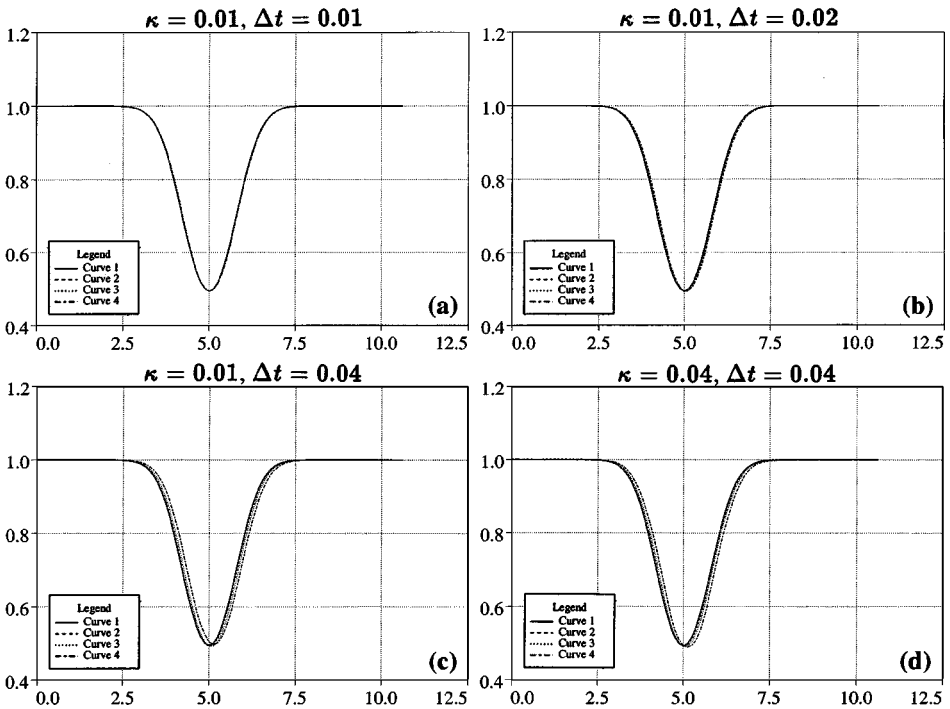

FIG. 4.1.4. Convecting vortex: Comparison of ACM66-ENT with the exact solution (solid line), illustrated by density profiles at the centerline $y = 0$, at $t = 100, 200, 300$ (curves 2–4) for $\Delta t = 0.01, 0.02, 0.04$ and $\kappa = 0.01$, and for $\Delta t = 0.04$ and $\kappa = 0.04$ on a 80×79 grid.

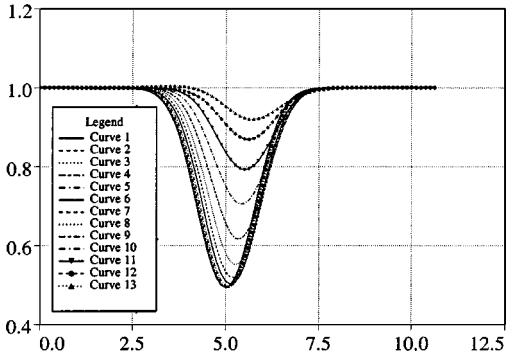

FIG. 4.1.5. Convecting vortex: Comparison of ACM66-ENT with the exact solution (left-most solid line), illustrated by density profiles at the centerline $y = 0$, at $t = 100,\ 200,\ 300,\ 400, 500, 600, 700, 800, 900, 1000, 1100, 1200$ for $\Delta t = 0.02$ and $\kappa = 0.01$ on a 80×79 grid. The left-most solid curve is the exact solution and the rest of the curves shifted to the right are the corresponding time sequences in an increasing order.

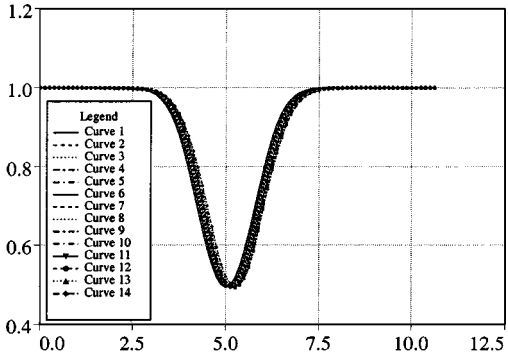

FIG. 4.1.6. Convecting vortex: Comparison of ACM66-ENT with the exact solution (left-most solid line), illustrated by density profiles at the centerline $y = 0$, at $t = 100,\ 200,\ 300,\ 400, 500, 600, 700, 800, 900, 1000, 1100, 1200, 1300$ for $\Delta t = 0.01$ and $\kappa = 0.01$ on a 80×79 grid. The left-most solid curve is the exact solution and the rest of the curves shifted to the right are the corresponding time sequences in an increasing order.

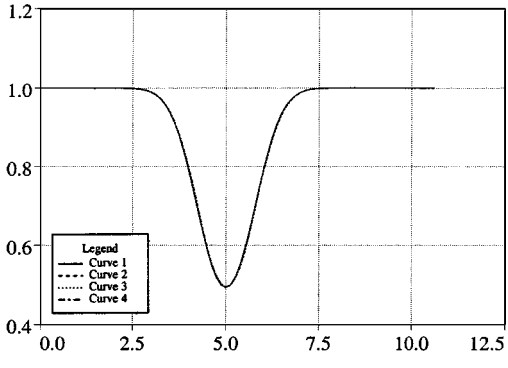

FIG. 4.1.7. Convecting vortex: Comparison of ACM66**S**-ENT with the exact solution (solid line), illustrated by density profiles at the centerline $y = 0$, at $t = 100, 200, 300$ (curves 2–4) for $\Delta t = 0.01$ and $\kappa = 0.005$ on a 80×79 grid.

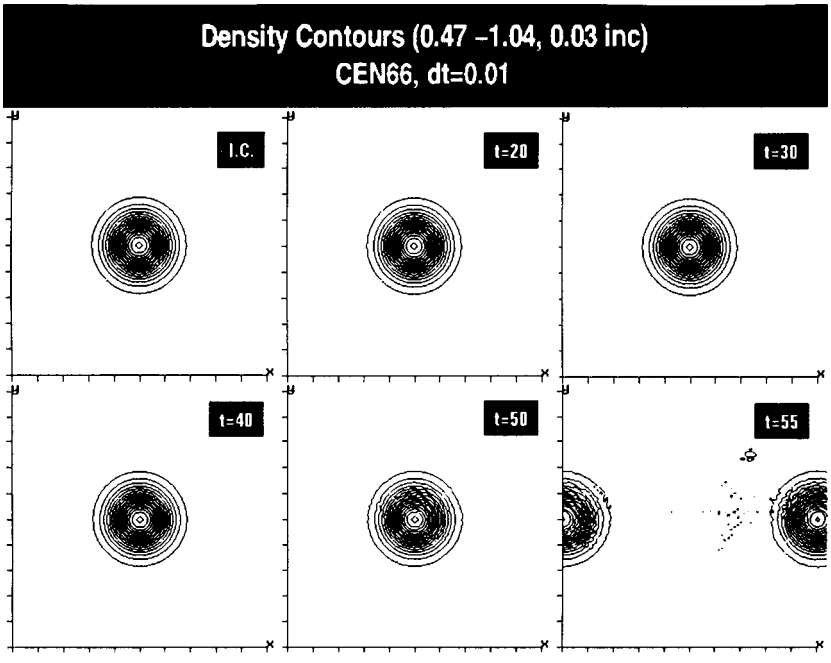

FIG. 4.1.8. Convecting vortex: Comparison of CEN66 with the exact solution (I.C.), illustrated by density contours at $t = 20, 30, 40, 50, 55$ for $\Delta t = 0.01$ on a 80×79 grid.

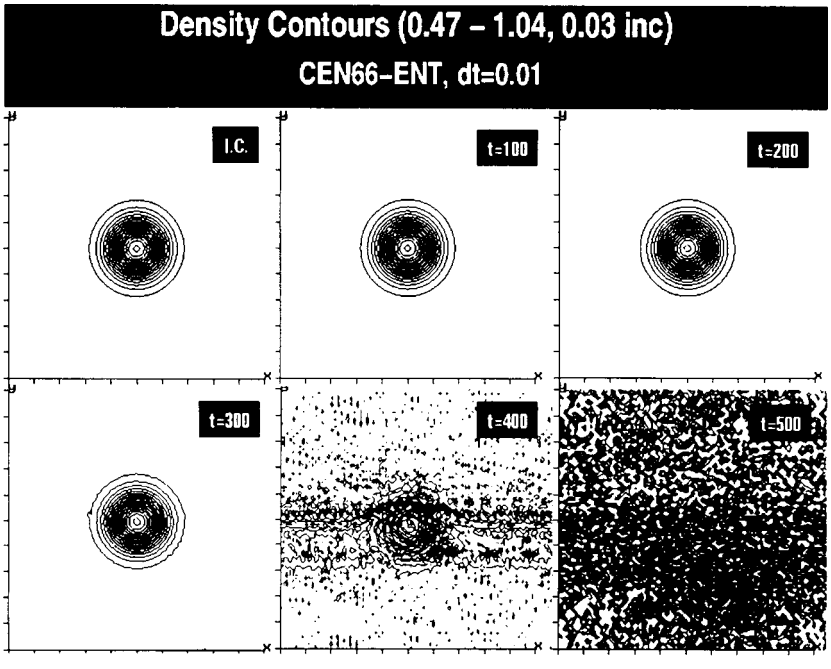

FIG. 4.1.9. Convecting vortex: Comparison of CEN66-ENT with the exact solution (I.C.), illustrated by density contours at $t = 100, 200, 300, 400, 500$ for $\Delta t = 0.01$ on a 80×79 grid.

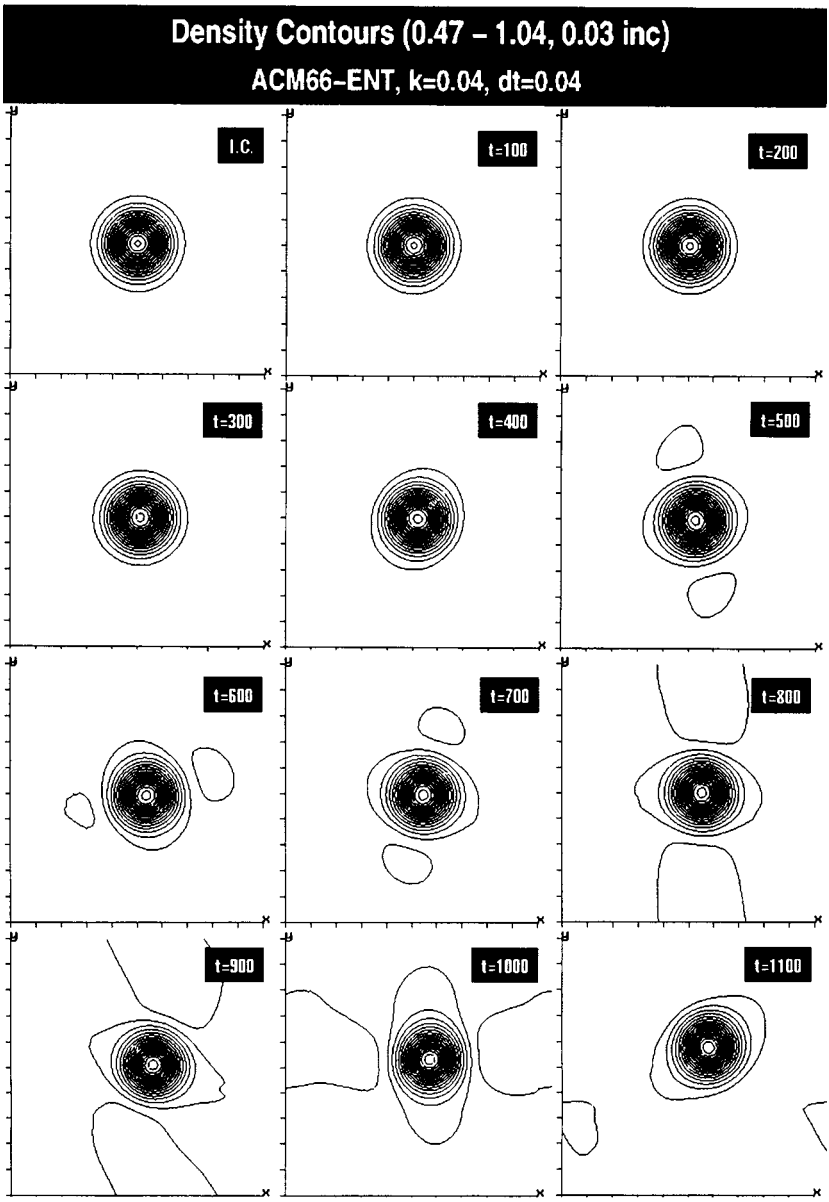

FIG. 4.1.10. Convecting vortex: Comparison of ACM66-ENT with the exact solution (I.C.), illustrated by density contours at $t = 100, 200, 300, 400, 500, 600, 700, 800, 900, 1000, 1100$ for $\Delta t = 0.04$ and $\kappa = 0.04$ on a 80×79 grid.

With the entropy splitting, the CEN22-ENT case diverged at 4.4 periods, the CEN44-ENT at 13 periods, and the CEN66-ENT at 17 periods for $\Delta t = 0.04$. The latter distribution is shown in Fig. 4.1.2c. Note that the entropy splitting allowed the calculation to proceed many periods further before it diverged, but, more significantly, the stability was improved as the order of accuracy was increased. This demonstrates the stabilizing effect of the entropy splitting. For a smaller $\Delta t = 0.01$, the CEN66-ENT is stable up to 53 periods. See the later discussions.

The addition of dissipation improved the performance markedly. Using the same $\Delta t = 0.04$, the ACM22 case with $\kappa = 0.07$ diverged after 10 periods, the ACM44 with $\kappa = 0.06$

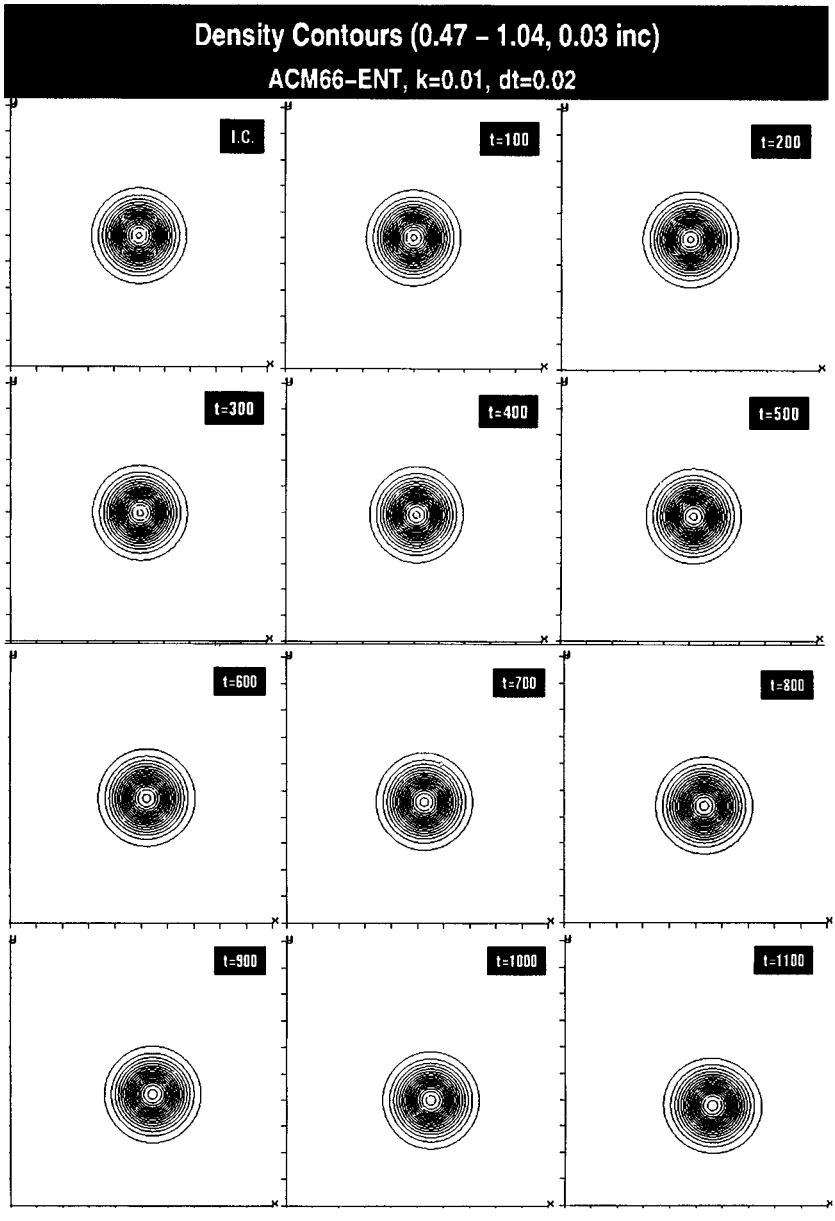

FIG. 4.1.11. Convecting vortex: Comparison of ACM66-ENT with the exact solution (I.C.), illustrated by density contours at $t = 100, 200, 300, 400, 500, 600, 700, 800, 900, 1000, 1100$ for $\Delta t = 0.02$ and $\kappa = 0.01$ on a 80×79 grid.

became very distorted after 40 periods (with $\kappa = 0.04$ diverged after 32 periods), and the ACM66 with $\kappa = 0.06$ remained stable for as long as we ran. (We stopped computing after 120 periods.) The density contours for this last case are shown in Fig. 4.1.12 of Yee *et al.* [19]. Note that the vortex center starts to drift vertically and horizontally, and undergoes gradual smearing and distortion starting at period 40 (see later discussion). The centerline distribution in Fig. 4.1.3c is therefore shown only up to period 30. The agreement with the exact solution is excellent.

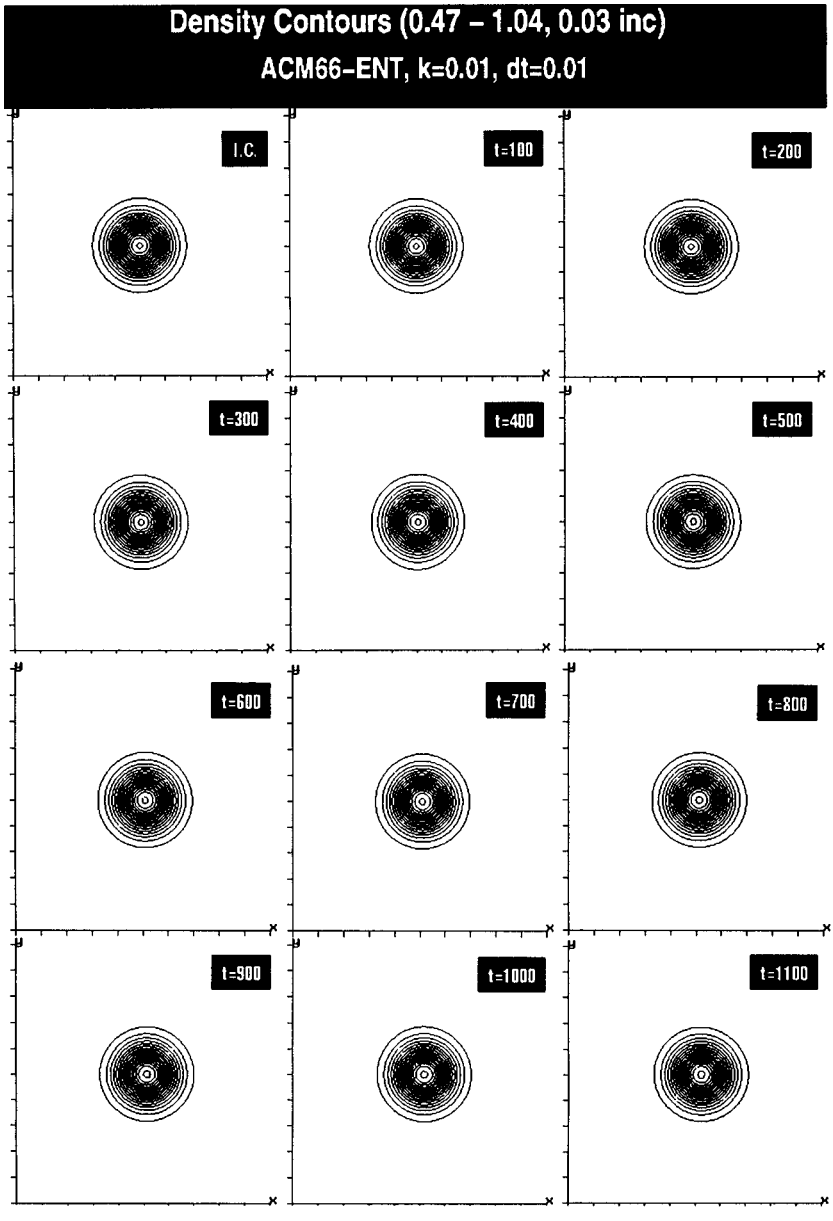

FIG. 4.1.12. Convecting vortex: Comparison of ACM66-ENT with the exact solution (I.C.), illustrated by density contours at $t = 100, 200, 300, 400, 500, 600, 700, 800, 900, 1000, 1100$ for $\Delta t = 0.01$ and $\kappa = 0.01$ on a 80×79 grid.

The addition of the entropy splitting yields further improvement. The ACM22-ENT with $\kappa = 0.07$ remained stable, but the solution became very distorted at 30 periods. The ACM44-ENT with $\kappa = 0.04$ similarly became severely distorted and drifted vertically and horizontally beyond 40 periods. The ACM66-ENT solution with $\kappa = 0.04$ remained very good up to period 120 (Fig. 4.1.10), although it started to drift to the right and upward even at period 30. This drift is evident from the centerline distributions in Fig. 4.1.4d.

(b) Effect of ACM dissipation. We first will compare sixth-order computational results without dissipation (CEN66) with those due to added second-order upwind dissipation (ACM66). Results without entropy splitting for $\Delta t = 0.04, 0.02$, and 0.01 are shown in Figs. 4.1.1 and 4.1.8 for CEN66, and Figs. 4.1.3 for ACM66. The CEN66 computations diverged shortly after five periods for all three time steps. The ACM66 computations remained stable for as long as we ran (120 periods) for all three time steps. Due to the drift of the vortex center, the centerline distributions in Fig. 4.1.3 are shown only up to 30 periods. Note that up to that time, the larger time step, $\Delta t = 0.04$ experienced less drift than the smaller time steps. The density contours for $\Delta t = 0.04$ show smearing and distortion as we increase the duration of the time integration.

Results with entropy splitting are shown in Figs. 4.1.2 and 4.1.9 for CEN66-ENT, and Figs. 4.1.4, 4.1.6, and 4.1.10–4.1.12 for ACM66-ENT. The entropy splitting for the non-dissipative computation (CEN66-ENT) allows a much longer time integration than that of CEN66 before it diverged, but even for the smallest time step, $\Delta t = .01$, the solution for CEN66-ENT deteriorated after 30 periods. Since ACM66-ENT allows a stable computation with less dissipation, the entropy splitting ($\kappa = 0.01$ and $\Delta t = 0.02, 0.01$) eliminated the distortion and smearing found in the ACM66 computations. The center of the vortex still drifted as we increased the time of the computation, but for the smallest time step, $\Delta t = 0.01$, there was only a very small drift to the right, even at 130 periods. Otherwise the vortex remained undistorted. Figures 4.1.5 and 4.1.6 show the centerline density distribution for 10–130 periods with a 10-period increment. One can see the drifting effect as a function of the Δt. Aside from the drifting, the vortex is still quite accurate. This is evident from the density contours Figs. 4.1.11 and 4.1.12.

We would like to point out that the vertical drifting of the vortex away from the centerline $y = 0$ and horizontal drifting (or rather shifting) are quite common for all schemes beyond 30 periods. Depending on the scheme, the amount of numerical dissipation and the time step, drifting can occur as early as 5 periods. We believe that the vertical drifting is due largely to the spatial numerical dissipation of the scheme. This is evident from the κ refinement study. See Figs. 4.1.10 and 4.1.12. The horizontal drifting is due largely to the phase error of the time integrator. This is evident from the time step refinement study on ACM66-ENT using $\kappa = 0.01$. See Figs. 4.1.5, 4.1.6, 4.1.11, and 4.1.12.

(c) Effect of the adjustable ACM parameter κ. Although we experimented with various values of κ ($0.01 \leq \kappa \leq 0.07$) to find the optimum value, we show some results only for the case giving the best solution, namely ACM66-ENT. For the larger time step, $\Delta t = 0.04$, Fig. 4.1.4 shows a negligible effect up to 30 periods when increasing the value of κ from 0.01 (Fig. 4.1.4c) to 0.04 (Fig. 4.1.4d). The computation $\kappa = 0.04$ and $\Delta t = 0.04$ remained stable, although with some distortion and smearing, as shown by the density contours in Fig. 4.1.10. Actually, this case gives slightly better results than the one using $\kappa = 0.01$ and the same time step size (not shown). The computation is not stable for $\kappa < 0.01$ and $\Delta t \geq 0.01$ for the ACM66-ENT scheme.

(d) Effect of entropy splitting. The cases discussed above clearly show the advantages of using entropy splitting. For the cases without dissipation, CEN66-ENT, the splitting allowed the computation to proceed for a much longer time before it became unstable. The real advantage came when used in conjunction with the upwind filter, ACM66-ENT, where excellent solutions with just a very small amount of drift were obtained after long time integrations of 130 periods.

(e) Effect of the time step. In general, decreasing the time step Δt gave a better solution. For the base scheme CEN66, the improvement in decreasing the time step from 0.04 to 0.01 was negligible. However, with entropy splitting, decreasing the time step had a significant effect, as seen from the results for CEN66-ENT in Figs. 4.1.2 and 4.1.9 and Figs. 4.1.10 of Yee *et al.* [19]. The improvement with decreasing time step was not as marked when the ACM filter was applied. (Figure 4.1.3 showing the density distributions for ACM66 actually appears to show an improvement with *increasing* time step. This is misleading, since the slight upward drift of the vortex center produced a shift in the centerline distributions for the smaller time steps. The density contours illustrate similar vortex preservation capability (not shown).) The improvement in decreasing the time step from 0.02 to 0.01 is clearly shown in the density distribution and density contours for ACM66-ENT of Figs. 4.1.5, 4.1.6, 4.1.11, and 4.1.12. The significant downward drift for $\Delta t = 0.02$ has been totally eliminated for $\Delta t = 0.01$. The drift to the right has also been virtually eliminated. A quantitative evaluation of the solution for $\Delta t = 0.01$ can be obtained from the centerline distribution for ACM66-ENT in Fig. 4.1.6. Even at 130 periods, the profile is undistorted, with a shift due to the small drift to the right.

(f) Effect of symmetric vs upwind ACM. We confine the comparison to the best solution, namely ACM66-ENT for $\Delta t = 0.01$. The centerline distributions up to period 30 for the symmetric ACM case, ACM66**S**-ENT in Fig. 4.1.7, are as good as for the upwind case, ACM66-ENT in Fig. 4.1.4a. The symmetric TVD dissipation of Yee [22, limiter 2.7b] was used. Note that the value of κ in the former case has been decreased to 0.005. A more meaningful comparison can be made by examining the density contours up to 110 periods for the two cases in Fig. 4.1.12 and Fig. 4.1.16 of Yee *et al.* [19]. The symmetric ACM solution undergoes some distortion and upward drift as the period is increased. Actually ACM66**S**-ENT with $\kappa = 0.005$ and $\Delta t = 0.01$ produced better results than ACM66-ENT with $\kappa = 0.04$ and $\Delta t = 0.01$ or $\kappa = 0.01$ and $\Delta t = 0.04$. The drifting behavior also occurs with ACM66-ENT if $\kappa \geq 0.04$ or for $\kappa = 0.01$ and $\Delta t = 0.04$. If we had used a larger value of $\kappa = 0.01$ for the symmetric case, the solution would have become very inaccurate. On the other hand, a smaller value of $\kappa = .001$ produced an unstable solution due to insufficient dissipation. It appears that the use of symmetric ACM filter in conjunction with entropy splitting is also computationally attractive. In all of the computations using ACM, the solution is quite sensitive to the value of κ and the time step size, although the upwind ACM appears to be a bit less sensitive.

(g) Effect of the splitting parameter β. All of the calculations shown for the entropy splitting have been for a value of $\beta = 1$ ($\alpha = -1.8$). This produces an equal amount of conservative and non-conservative splitting. We have also run some cases for $\beta = 0.5$ ($\alpha = -1.6$). This gives a splitting that is one-third conservative and two-thirds non-conservative. The results are slightly worse than for the $\beta = 1$ case. Increasing the conservative proportion beyond 80% will defeat the purpose of using the splitting for this particular example since the gain in stability is diminished by the expense of the added CPU computation required by the splitting.

In summary, the use of entropy splitting in conjunction with an upwind TVD ACM filter has preserved a horizontally convecting vortex with great accuracy after long time integration of 130 periods. The splitting helps minimize the use of numerical dissipation. To the authors' knowledge, highly accurate finite discretization computations previously reported in the literature were only carried out up to 10 periods of integration.

4.2. *Vortex Pairing in a Time-Developing Mixing Layer*

This test case involved vortex growth and pairing in a temporal mixing layer at a convective Mach number equal to 0.8. At this Mach number there are shock waves (shocklets) that form around the vortices and the problem is to compute accurately the vortex evolution while avoiding oscillations around the shocks. Previous calculations of the problem can be found in [13, 41–45]. Figure 4.2.1 shows a schematic of the physical problem. Here we set up a base flow as in Sandham and Yee [45]

$$u = 0.5 \tanh(2y), \tag{4.2.1}$$

with velocities normalized by the velocity jump $u_1 - u_2$ across the shear layer and distances normalized by the vorticity thickness,

$$\delta_\omega = \frac{u_1 - u_2}{(du/dy)_{max}}. \tag{4.2.2}$$

Subscripts 1 and 2 refer to the upper ($y > 0$) and lower ($y < 0$) streams of fluid, respectively. The normalized temperature and hence local sound speed squared is determined from an assumption of constant stagnation enthalpy

$$c^2 = c_1^2 + \frac{\gamma - 1}{2}\left(u_1^2 - u^2\right). \tag{4.2.3}$$

Equal pressure through the mixing layer is assumed. Therefore, for this configuration of $u_2 = -u_1$ both fluid streams have the same density and temperature for $y \to \pm\infty$. The Reynolds number defined by the velocity jump, vorticity thickness, and kinematic viscosity at the freestream temperature is set equal to 1000. The Prandtl number is set to 0.72, the ratio of specific heats is taken as $\gamma = 1.4$, and Sutherland's law with reference temperature $T_R = 300^\circ$ K is used for the viscosity variation with temperature. The reference sound speed squared, c_R^2, is taken as the average of c^2 over the two free streams.

Disturbances are added to the velocity components in the form of simple waves. For the normal component of velocity we have the perturbation

$$v' = \sum_{k=1}^{2} a_k \cos(2\pi k x / L_x + \phi_k) \exp(-y^2/b), \tag{4.2.4}$$

where $L_x = 30$ is the box length in the x-direction and $b = 10$ is the y-modulation. In our test case we simulate pairing in the center of the computational box, by choosing the initially most unstable wave $k = 2$ to have amplitude $a_2 = 0.05$ and phase $\phi_2 = -\pi/2$, and the subharmonic wave $k = 1$ with $a_1 = 0.01$ and $\phi_1 = -\pi/2$. The u-velocity perturbations are found by assuming that the total perturbation is divergence free. Even though these fluctuations correspond only approximately to eigenfunctions of the linear stability problem for a compressible mixing layer, they serve the purpose of initiating the instability of the mixing layer and have the advantage as a test case in that they can be easily coded.

Numerically the grid is equally spaced and periodic in the x-direction and stretched in the y-direction, using the mapping

$$y = \frac{L_y}{2} \frac{\sinh(b_y \eta)}{\sinh(b_y)}, \tag{4.2.5}$$

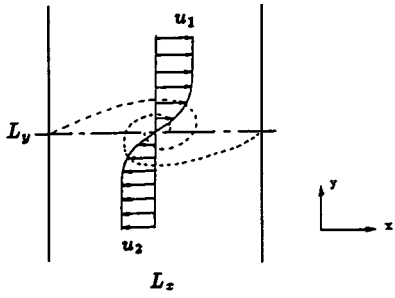

FIG. 4.2.1. Schematic of the vortex pairing in a time-developing mixing layer.

where we take the box size in the y-direction $L_y = 100$, and the stretching factor $b_y = 3.4$. The mapped coordinate η is equally spaced and runs from -1 to $+1$. The boundaries at $\pm L_y/2$ are taken to be slip walls. For example, at the lower boundary

$$\rho_1 = \rho_2, \tag{4.2.6a}$$

$$(\rho u)_1 = (\rho u)_2, \tag{4.2.6b}$$

$$(\rho v)_1 = 0, \tag{4.2.6c}$$

$$(e)_1 = [4(e)_2 - (e)_3]/3, \tag{4.2.6d}$$

where subscripts here refer to the grid point and e is the total energy.

We compute this test case on a 101×101 grid. A grid refinement study was performed in [13]. Figure 4.2.2, a reference solution taken from Yee *et al.* [13] using ACM44, shows a

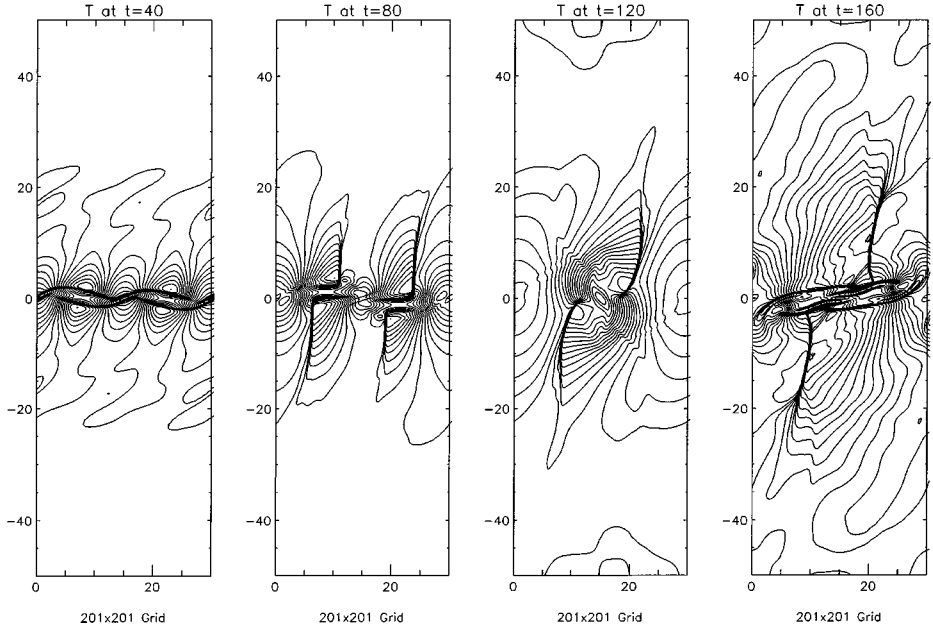

FIG. 4.2.2. Vortex pairing: Four stages in the vortex pairing, at times $t = 40, 80, 120, 160$, showing the normalized temperature contours for a 201×201 grid with $\kappa = 0.7$ for the nonlinear fields and $\kappa = 0.35$ for the linear fields using ACM44.

snapshot of the temperature contours at $t = 40$, 80, 120, and 160 using ACM44, illustrating the roll-up of the primary vortices followed by vortex merging. Shock waves and shears form around the vortices with a peak Mach number ahead of the vortex of approximately 1.55 at $t = 120$. The grid is 201×201.

For this vortex pairing in a time-developing mixing layer, we study only the effect of the choice of the arbitrary splitting parameter β (i.e., the proportion of conservative and non-conservative parts of the splitting) in obtaining the same shock location as the un-split approach with scheme ACM66-ENT using $\Delta t = 0.1$. In all of the computations for the vortex pairing case, limiter (2.25h), and $\delta = 0.25$ (2.26a) of [13] are used and $\kappa = 0.7$ (2.4.2) is used for the nonlinear fields for the ACM methods. An intermediate BC update is imposed in order to have a one-to-one comparison with the Yee *et al.* [13] results.

We consider $\alpha = -100, -10, -5, -3, -2, -1.8$ ($\beta = 1$), $-1.6, 0.1, 1$ ($\beta = -6$), 2, 5, 10, 100 with $\beta = (\alpha + \gamma)/(1 - \gamma)$. The scheme diverges for $\alpha = 0.1$. This corresponds to 136.36% of the conservative proportion and -36.36% the non-conservative proportion.

By monitoring the left λ-shock location, studies indicate that for $\alpha > |5|$, the same shock location and shock strength of the λ-shock are obtained as in the un-split approach. With the exception of a small increase in spurious noise in the vicinity of the shock (not shown), it is surprising to see that a slightly over 100% conservative proportion ($\alpha > 0$) and the corresponding negative non-conservative proportion would give the correct shock strength and location. Away from the λ-shock area, the solution is less sensitive to the choice of $\alpha > |5|$.

For the physical choice of $\alpha < -\gamma$, we obtain the opposite effect as compared to that of $\alpha > 0$, in terms of spurious noise. As $\alpha \to 1 - 2\gamma$, the entropy splitting has a spurious noise reduction capability when compared with the un-split approach. For example, the shock strength and location that are a bit away from the λ-shock are almost the same for $\alpha = -3$ ($\beta = 4$) as for $\alpha = -5$ ($\beta = 9$), except that $\alpha = -3$ has a bigger smoothing effect on the spurious noise generated by the scheme (especially when a more compressive flux limiter is employed). In addition, for $-5 < \alpha < -\gamma$, a bigger negative α in that range results in more shift of the λ-shock location away from the un-split approach location. For example, for $\alpha = -3$, there is a shift of approximately $1 - 1\,1/2$ grid points. The shock strength reduction at the λ-shock location is very small. A reduction in Δt might improve the accuracy of the shift in the shock location, based on the vortex convection case. Here, we only compare the results with the un-split approach using the same time step and BCs as reported in [13]. Figure 4.2.3 illustrates the normalized temperature at $t = 160$ using $\alpha = -5$ and $\alpha = -3$ on a 101×101 grid. Except for a slight noise reduction in the vicinity of the shock, the $\alpha = -5$ solution is almost identical to the un-split computation. To illustrate the noise reduction capability of the splitting, Fig. 4.2.4 shows a comparison of the split and un-split forms with the ACM filter turned off for the linearly degenerate fields (u, u and v, v characteristic fields) using $\alpha = -3$ ($\beta = 4$). One can see the noise reduction effect of the entropy splitting on the scheme which, at the same time, maintains the accuracy of the shock and shears away from the λ-shock location as in the un-split approach. Since the entropy splitting requires the same amount of filter as the un-split approach for this type of rapidly developing shock-turbulence interactions, its stabilizing effect is only on the spurious noise reduction, and the benefit is not as pronounced as for the smooth flow case. Followup studies by Sandham and Yee [16], Hadjadj *et al.* [17] and Yee *et al.* [46] reveal that for turbulent flows involving long time integrations that contain weak or no shock waves, the entropy splitting can minimize the use of numerical dissipation due to its unique nonlinear stability property.

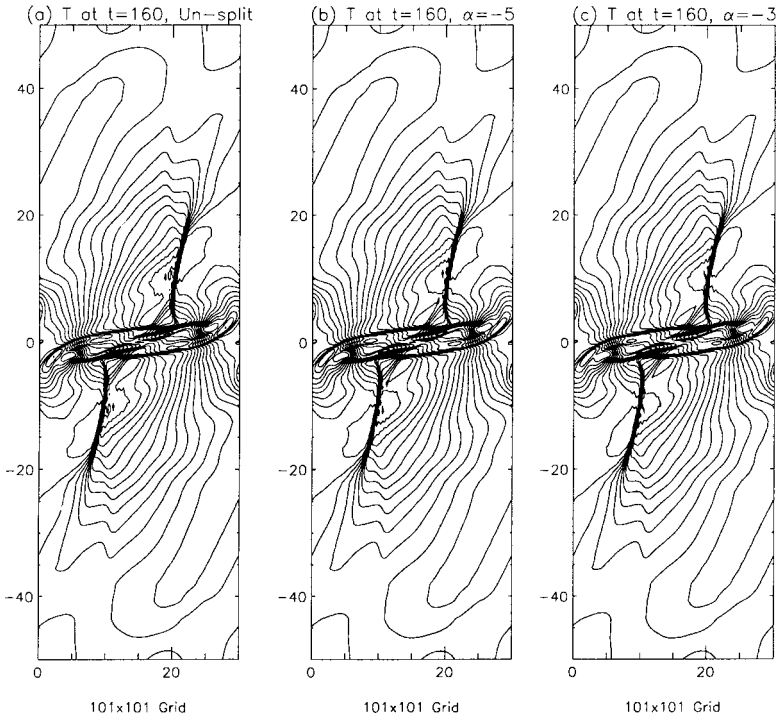

FIG. 4.2.3. Vortex pairing: Comparison of normalized temperature contours for $\alpha = -5$ and -3 with the un-split approach at time $t = 160$ on a 101×101 grid with $\kappa = 0.7$ for the nonlinear fields and $\kappa = 0.35$ for the linear fields using ACM66.

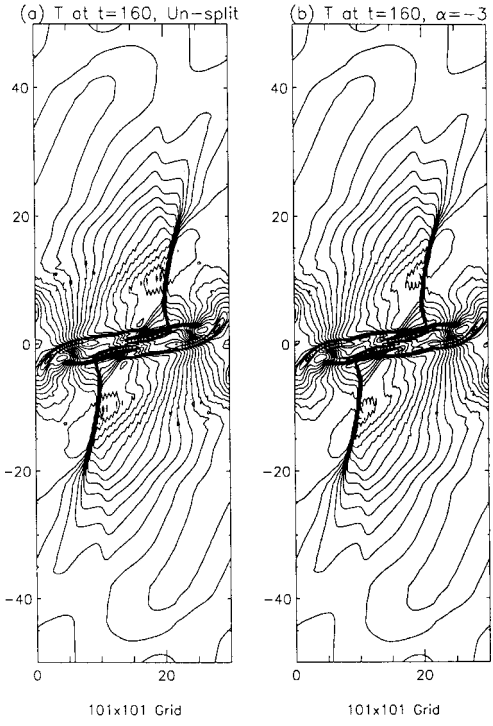

FIG. 4.2.4. Vortex pairing: Comparison of normalized temperature contours for $\alpha = -3$ with the un-split approach at time $t = 160$ on a 101×101 grid with $\kappa = 0.7$ for the nonlinear fields and $\kappa = 0$ for the linear fields using ACM66.

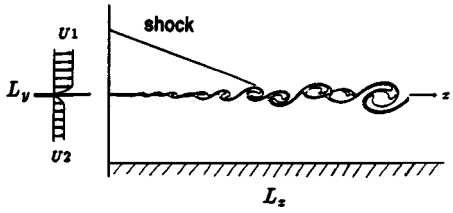

FIG. 4.3.1. Schematic of the shock impingement on a spatially developing mixing layer.

4.3. *Shock Wave Impingement on a Spatially Evolving Mixing Layer*

The third test case has been developed to test the behavior of the schemes for shock waves interacting with shear layers where the vortices arising from shear layer instability are forced to pass through a shock wave. Figure 4.3.1 shows the schematic of the physical problem. An oblique shock is made to impact on a spatially developing mixing layer at an initial convective Mach number of 0.6. The shear layer vortices pass through the shock system and later through another shock, imposed by reflection from a (slip) wall at the lower boundary. The problem has been arranged with the Mach number at the outflow boundary everywhere supersonic so that no explicit outflow boundary conditions are required. This allows us to focus on properties of the numerical schemes rather than on the boundary treatment.

Figure 4.3.2, a reference solution taken from Yee *et al.* [13] using ACM44, shows the nature of the flow on a 641×161 grid illustrating the pressure, density, and temperature

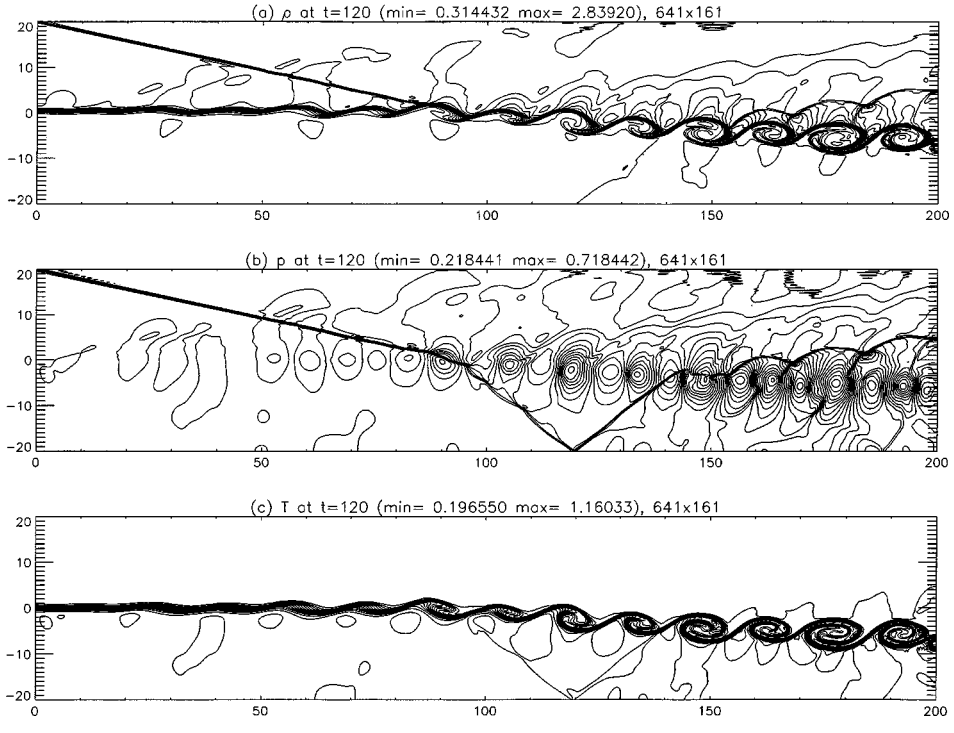

FIG. 4.3.2. Shock-shear-layer interaction: The reference solution at $t = 120$ using ACM44. Contours are shown of (a) density, (b) pressure, and (c) normalized temperature for a 641×161 grid with $\kappa = 0.35$ for the nonlinear fields and $\kappa = 0.175$ for the linear fields.

fields using the ACM44 method and the same limiter as the pairing case with $\kappa = 0.35$ for nonlinear characteristic fields and $\kappa = 0.175$ for linear characteristic fields. The time step is $\Delta t = 0.12$. The entropy satisfying parameter δ of Harten and Hyman [40] is set to 0.25. An oblique shock originates from the top left hand corner and this impacts on the shear layer at around $x = 90$. The shear layer is deflected by the interaction. Afterwards we have a shock wave below the shear layer and an expansion fan above it. The shock wave reflects from the lower solid wall and passes back through the shear layer. The lower wall uses a slip condition so no viscous boundary layer forms and we focus on the shock-wave interaction with the unstable shear layer.

The inflow is specified again with a hyperbolic tangent profile, this time as

$$u = 2.5 + 0.5 \tanh(2y), \tag{4.3.1}$$

giving a mixing layer with upper velocity $u_1 = 3$, lower velocity $u_2 = 2$, and hence a velocity ratio of 1.5. Equal pressures and stagnation enthalpies are assumed for the two streams, with convective Mach number, defined by

$$M_c = \frac{u_1 - u_2}{c_1 + c_2}, \tag{4.3.2}$$

equal to 0.6 c_1 and c_2 are the freestream sound speeds. The reference density is taken as the average of the two free streams and a reference pressure as $(\rho_1 + \rho_2)(u_1 - u_2)^2/2$. This allows one to compute the inflow parameters as given in the first two columns of Table II. Inflow sound speed squared is found from the relation for constant stagnation enthalpy (4.2.3). The θ in Table II is the flow inclination angle with respect to the x-direction.

The upper boundary condition given in column 3 of Table II is taken from the flow properties behind an oblique shock with angle $\tilde{\beta} = 12^\circ$. The table also gives the properties behind the expansion fan (column 4) and after the oblique shock on the lower stream of fluid (column 5) computed by standard gasdynamics methods with $\tilde{\beta} = 38.118^\circ$. In practice, the conditions in regions 4 and 5 do not correspond exactly to the simulations due to the finite thickness of the shear layer. The Mach number of the lower stream after this shock is approximately $M_5 = 1.6335$ and remains supersonic through all the successive shocks and expansion fans up to the outflow boundary. The resulting shock waves are not strong, but tests showed that

TABLE II
Flow Properties for the Shock-Wave/Shear-Layer Test Case in Various Regions of the Flow

Property	(1)	(2)	(3)	(4)	(5)
u-velocity	3.0000	2.0000	2.9709	2.9792	1.9001
v-velocity	0.0000	0.0000	−0.1367	−0.1996	−0.1273
θ (degrees)	0.0000	0.0000	2.6343	3.8330	3.8330
Density ρ	1.6374	0.3626	2.1101	1.8823	0.4173
Pressure ρ	0.3327	0.3327	0.4754	0.4051	0.4051
Sound speed c	0.5333	1.1333	0.5616	0.5489	1.1658
Mach number $\lvert M \rvert$	5.6250	1.7647	5.2956	5.4396	1.6335

Note. (1) Upper stream inflow, (2) lower stream inflow, (3) upper stream after oblique shock, (4) upper stream after expansion fan, (5) lower stream after shock wave.

they could not be computed without using shock-capturing techniques. The lower boundary was specified with the same slip condition used for the pairing case (Eq. (4.2.6)).

The Prandtl number and ratio of specific heats were taken to be the same as for the vortex pairing test case. The Reynolds number was chosen to be 500. Fluctuations are added to the inflow as

$$v' = \sum_{k=1}^{2} a_k \cos(2\pi kt/T + \phi_k) \exp(-y^2/b), \tag{4.3.3}$$

with period $T = \lambda/u_c$, wavelength $\lambda = 30$, convective velocity $u_c = 2.68$ (defined by $u_c = (u_1c_2 + u_2c_1)/(c_1 + c_2)$) and $b = 10$. For $k = 1$ we take $a_1 = 0.05$ and $\phi = 0$, and for $k = 2$ we take $a_2 = 0.05$ and $\phi = \pi/2$. No perturbations are added to the u-component of velocity.

The grid is taken to be uniform in x and stretched in y according to Eq. (4.2.5) with $b_y = 1$. This stretching is much milder than for the pairing problem, as we have to resolve the shear layer even when it deflects away from $y = 0$. The box lengths were taken to be $L_x = 200$ and $L_y = 40$.

The reference solution indicates that vortex cores are located by low pressure regions and the stagnation zones between vortices by high pressure regions. The shock waves are seen to be deformed by the passage of the vortices. Another interesting observation is the way the core of the vortex at $x = 148$ has been split into two by its passage through the reflected shock wave. In spite of the relatively high amplitude chosen for the subharmonic inflow perturbation, there is no pairing of vortices within the computational box. We do, however, begin to see eddy shock waves around the vortices near the end of the computational box where the local convective Mach number has increased to around 0.66. The oscillations seen near the upper boundary for $x > 120$ occur where the small Mach waves from the initial perturbations arrive at the upper boundary. The use of characteristic boundary conditions should remove this problem. Practically, the amplitude of oscillations is not sufficient to cause numerical instability or affect the remainder of the flow.

For this shock wave impingement on a spatially evolving mixing layer, again, we study only the effect of the choice of the arbitrary splitting parameter β in obtaining the same shock location as the un-split approach. The study is limited to ACM66-ENT and ACM66 using the fifth limiter of Eq. (2.25h) of [13], and the same κ value and time step size ($\Delta t = 0.12$) as the reference solution. Intermediate BC updates are imposed in order to have a one-to-one comparison with the Yee *et al.* [13] result. We consider $\alpha = -100, -10, -5, -3, -2, -1.8$ ($\beta = 1$), $-1.6, 0.1, 1 (\beta = -6), 2, 3, 4, 5, 10, 20, 100$. Studies indicate that for $\alpha = -2, -1.8, -1.6, 0.1, 1, 2, 3, 4, 5$ the solution diverges. The rest of the α values for $|\alpha| \geq 10$ produce almost identical results as the un-split case. This example poses a more stringent requirement on the α range than the vortex pairing case. Figure 4.3.3 compares the un-split pressure contours with the split case for $\alpha = \pm 10$ at $t = 120$ on a 321×81 grid with $\Delta t = 0.12$. The value of $\alpha = +10$ ($\beta = -28.5$) corresponds to a 103.6% conservative proportion and a small negative non-conservative proportion. The $\alpha = -10$ ($\beta = 21.5$) corresponds to a less than 100% conservative proportion. Note that the $\alpha = -10$ solution produces spurious noise reduction, while the $\alpha = +10$ solution actually induces more spurious noise than the un-split approach. This opposite effect of the spurious noise phenomena for $\alpha > 0$ and $\alpha < -\gamma$ is shared with the vortex pairing example. Again, for turbulent flows involving long time integrations that contain weak or no shock waves, entropy splitting can minimize the use of numerical dissipation due to its unique nonlinear stability property [16, 17, 46].

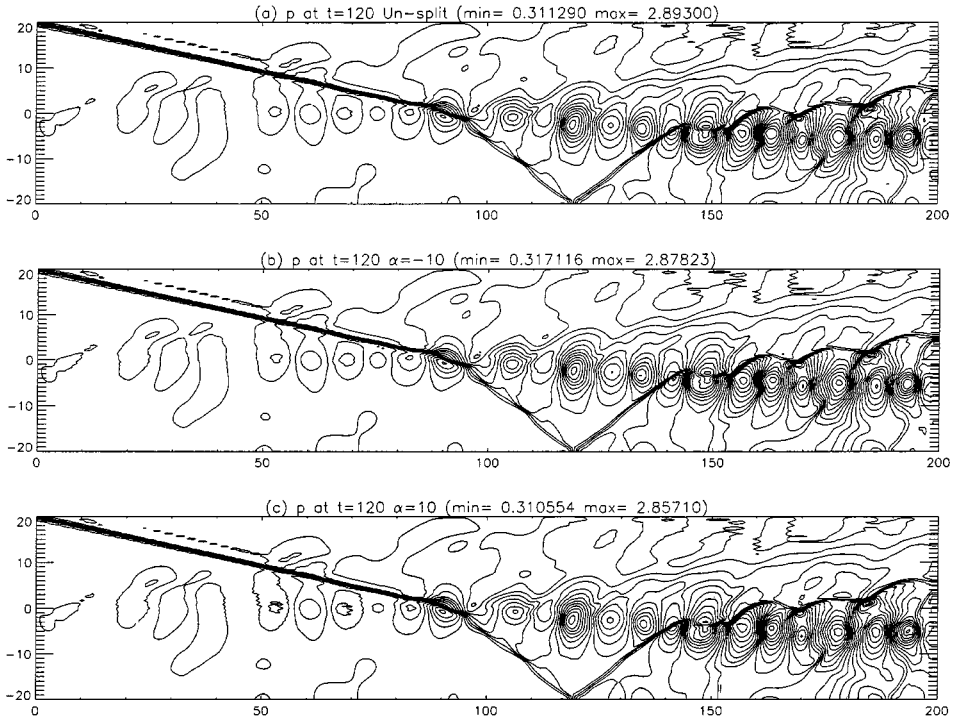

FIG. 4.3.3. Shock-shear-layer interaction: Comparison of the pressure contours for $\alpha = \pm 10$ with the un-split approach using ACM66 at $t = 120$ on a 321×81 grid with $\kappa = 0.35$ for the nonlinear fields and $\kappa = 0.175$ for the linear fields.

4.4. *Computational Costs*

For the compressible mixing layer computations using the fourth-order Runge–Kutta method, the central base schemes with the ACM filter are only around 25% more expensive than the same base schemes without ACM filter. This has been achieved by only requiring one application of the ACM filter per full time step for the convection terms. For LMM time discretizations, the central base scheme with the ACM filter is only 10% more expensive than standard second-order TVD schemes. The entropy splitting is approximately 20% more expensive than the un-split conservative form for the 2-D mixing layer computations in conjunction with the fourth-order Runge–Kutta method. The extra CPU time is mainly due to the fact that, for each direction, four entropy splittings are required. If two to three time level LMM types of time discretizations are used, less CPU time can be realized.

SUMMARY

Our study shows that the entropy splitting can be formally extended to a thermally perfect gas, with the internal energy being an arbitrary function of temperature. For nonequilibrium flows which consist of a mixture of different species, each obeying a thermally perfect gas law, extension of the splitting is problematic. While we were able to prove the symmetry and homogeneity properties, the degree of homogeneity can only be obtained by solving a system of nonlinear equations. In addition, to obtain the Jacobian of the transformation required inverting a non-sparse linear system. It would therefore be difficult to establish the positive definite condition. Consequently, the extension of the method to nonequilibrium

flows is not practically feasible. If the homogeneity condition is not required, then one can use symmetry variables based on the physical entropy, as was shown by Chalot *et al.* [37]. In this case, the resulting PDEs are in pure non-conservative form and entropy splitting is no longer possible. For magnetohydrodynamics, the magnetic field has to be added as a "conservative" variable. But the square of the magnetic field is one of the terms in the definition of the total energy. Thus, from dimensional arguments it is clear that one cannot obtain the homogeneity condition. A similar situation exists for the artificial compressibility method of treating incompressible flow.

Using the same high order central schemes, numerical experiments with a 2-D vortex convection Euler computation consisting of periodic BCs indicate that entropy splitting is more stable than the un-split (purely conservative) approach. With an appropriate time step, numerical dissipation is not required for up to 30 spatial periods with nearly perfect vortex preservation as opposed to only 5 periods for its un-split cousin. For even longer time integration, although numerical dissipation is needed to stabilize the schemes, the amount required is much less than for its un-split cousin. A nearly perfect vortex preservation of up to 130 periods was achieved.

For the mixing layer study, in order to obtain the same λ-shock strength and shock location as the un-split approach using the same scheme, the range of the arbitrary splitting parameter β has to be confined to the use of at least 90% of the conservative proportion of the flux derivative. For problems without λ-shocks, a wider range of β can be used. Only a slight advantage of the entropy splitting over the un-split approach was observed for this type of flow physics. The advantage is in terms of noise reduction and improved nonlinear stability. There is no reduction in the use of the ACM filter. This might largely be due to the rapidly developing flow and the high percentage of conservative proportion required. Perhaps replacing the ACM sensor by the wavelet sensor [15] in conjunction with moderate grid adaptation could help improve the situation. Unlike the vortex convection with periodic BCs in all spatial directions, these two more complicated cases consist of rapidly developing flows. Not all of the physical BCs are periodic. In addition, the BCs consist of spatially or temporally sinusoidal disturbances. Thus, the performance of the schemes for the mixing layer cases is partially clouded by the spatially and temporally dependent physical BCs that required special treatment in conjunction with the Runge–Kutta time integrator, and also by the fact that we did not impose the more stable and appropriate boundary difference operator. The use of the symmetric form of Harten [10] for the viscous term might be a source of improvement. In addition, a time step reduction will also benefit the use of entropy splitting as indicated in the vortex convection study. Without additional study, the benefit of using the entropy splitting is inconclusive for compressible turbulence mixing applications. Since the entropy splitting requires the same amount of filter as the un-split approach for rapidly developing shock-turbulence interactions, its stabilizing effect is not as pronounced as for the smooth flow case. However, for turbulent flows involving long time integrations that contain weak or no shock waves, the entropy splitting could help minimize the use of numerical dissipation due to its unique nonlinear stability property. More rigorous implementation of the BCs and extensive study are needed. See [15–17, 46] for followup studies.

Overall, the three numerical examples indicate a positive benefit of the entropy splitting. The splitting can stabilize spurious noise generated by the non-dissipative or low dissipative spatial discretizations which are a major cause of nonlinear instability. Modern high-resolution numerical dissipation has been the major player in improving nonlinear

instabilities for short or moderate time integrations (unsteady). Most often, added numerical dissipation is necessary for longer time integration at the expense of excess smearing of the flow physics without resorting to finer grids and extremely small time steps. The use of the entropy splitting form of the flux derivative in conjunction with high-resolution filters can minimize the use of numerical dissipation. We believe that the use of the entropy splitting is not limited to spatial central schemes (compact or non-compact), but to spectral and spectral-like spatial schemes as well. This and the blending of ACM or wavelet filters with other filters on the possible suppression of spurious high frequency oscillations as discussed in Subsection 2.6 are the subjects of our near future research.

ACKNOWLEDGMENTS

Special thanks to Tom Coakley and Dennis Jespersen for their critical review of the manuscript. Thanks also to Cetin Kiris for his help in the graphics illustrations.

REFERENCES

1. H.-O. Kreiss and G. Scherer, *On the Existence of Energy Estimates for Difference Approximations for Hyperbolic Systems*, Technical Report, Department of Scientific Computing, Uppsala University, 1977.
2. B. Strand, Summation by parts for finite difference approximations for d/dx, *J. Comput. Phys.* **110**, 47 (1994).
3. P. Olsson, Summation by parts, projections and stability, *Math. Comp.* **64**, 1035 (1995).
4. B. Gustafsson and P. Olsson, Fourth-order difference method for hyperbolic IBVPs, *J. Comput. Phys.* **1177**, 300 (1995).
5. P. Olsson and J. Oliger, *Energy and Maximum Norm Estimates for Nonlinear Conservation Laws*, RIACS Technical Report 94-01, NASA Ames Research Center, 1994.
6. P. Olsson, Summation by parts, projections and stability, II, *Math. Comp.* **64**, 212 (1995).
7. P. Olsson, *Summation by Parts, Projections and Stability, III*, RIACS Technical Report 95-06, NASA Ames Research Center, 1995.
8. M. Gerritsen, *Designing an Efficient Solution Strategy for Fluid Flows*, Ph.D. Thesis, SCCM Program, Stanford University, October 1996.
9. M. Gerritsen and P. Olsson, Designing an efficient solution strategy for fluid flows. I. A stable high order finite difference scheme and sharp shock resolution for the Euler equations, *J. Comput. Phys.* **129**, 245 (1996).
10. A. Harten, *On the Symmetric Form of Systems for Conservation Laws with Entropy*, ICASE Report 81-34, NASA Langley Research Center, 1981; *J. Comput. Phys.* **49**, 151 (1983).
11. J. L. Steger and R. F. Warming, Flux vector splitting of inviscid gas dynamics equations with applications to finite difference methods, *J. Comput. Phys.* **40**, 263 (1981).
12. R. J. R. Hughes, L. P. Franca, and M. Mallet, A new finite element formulation for computational fluid dynamics. I. Symmetric forms of the compressible Euler and Navier–Stokes equations and the second law of thermodynamics, *Comput. Methods Appl. Mech. Eng.* **54**, 223 (1986).
13. H. C. Yee, N. D. Sandham, and M. J. Djomehri, *Low Dissipative High Order Shock-Capturing Methods Using Characteristic-Based Filters*, RIACS Technical Report 98.11, May 1998; *J. Comput. Phys.* **150**, 199 (1999).
14. A. Harten, The artificial compression method for computation of shocks and contact discontinuities. III. Self-adjusting hybrid schemes, *Math. Comp.* **32**, 363 (1978).
15. B. Sjogreen and H. C. Yee, *Multi-Resolution Wavelet Based Adaptive Numerical Dissipation Control for Shock-Turbulence Computations*, RIACS Technical Report, NASA Ames Research Center, 2000.
16. N. D. Sandham and H. C. Yee, *Entropy Splitting for High Order Numerical Simulation of Compressible Turbulence*, RIACS Technical Report, NASA Ames Research Center, 2000; Proceedings of the 1st International Conference on CFD, July 10–14, 2000, Kyoto, Japan.

17. A. Hadjadj, H. C. Yee, and N. D. Sandham, *Comparison of WENO with Low Dissipative High Order Schemes for Compressible Turbulence Computations*, RIACS Technical Report, NASA Ames Research Center, 2000.
18. M. Vinokur and H. C. Yee, *Extension of Efficient Low Dissipative High Order Schemes for 3-D Curvilinear Moving Girds*, NASA Technical Memorandum, NASA Ames Research Center, 2000; Proceedings of the Computing the Future III: Frontier of CFD, June 26–28, 2000, Half Moon Bay, CA.
19. H. C. Yee, M. Vinokur, and M. J. Djomehri, *Entropy Splitting and Numerical dissipation*, NASA Technical Memorandum 208793, NASA Ames Research Center, 1999.
20. G. Dahlquist, Some properties of linear multistep and one-leg methods for ordinary differential equations, in *Conference Proceeding, 1979 SIGNUM Meeting on Numerical ODE's, Champaign, IL*, 1979.
21. H. C. Yee and A. Harten, *Implicit TVD Schemes for Hyperbolic Conservation Laws in Curvilinear Coordinates*, AIAA Paper No. 85-1513, Proceedings of the AIAA 7th CFD Conference, Cinncinati, OH, July 1985; *AIAA J.* **25**, 266 (1987).
22. H. C. Yee, On symmetric and upwind TVD schemes, in *Proceedings of the 6th GAMM-Conference on Numerical Methods in Fluid Mechanics, Gottingen, Germany*, September 1985.
23. H. C. Yee, Linearized form of implicit TVD schemes for multidimensional Euler and Navier–Stokes equations, *Comput. Math. Appl. A* **12**, 413 (1986).
24. H. C. Yee, Construction of explicit and implicit symmetric TVD schemes and their applications, *J. Comput. Phys.* **68**, 151 (1987).
25. H. C. Yee, *A Class of High-Resolution Explicit and Implicit Shock-Capturing Methods*, VKI Lecture Series 1989-04 March 6–10, 1989; also NASA TM-101088, February 1989.
26. H. C. Yee, G. H. Klopfer, and J.-L. Montagne, High-resolution shock-capturing schemes for inviscid and viscous hypersonic flows, *J. Comput. Phys.* **88**, 31 (1990).
27. A. Harten, A high resolution scheme for computation of weak solutions of hyperbolic conservation laws, *J. Comput. Phys.* **49**, 35 (1983).
28. R. M. Beam and R. F. Warming, An implicit finite-difference algorithm for hyperbolic systems in conservation law form, *J. Comput. Phys.* **22**, 87 (1976).
29. R. Vichnevetsky, *Numerical Filtering for Partial Differencing Equations*, Numerical Applications Memorandum, Rutgers University, NAM 156, 1974.
30. P. Alpert, Implicit filtering in conjunction with explicit filtering, *J. Comput. Phys.* **44**, 212 (1981).
31. S. A. Lele, Compact finite difference schemes with spectral-like resolution, *J. Comput. Phys.* **103**, 16 (1992).
32. M. R. Visbal and D. V. Gaitonde, *High-Order Accurate Methods for Unsteady Vortical Flows on Curvilinear Meshes*, AIAA Paper 98-0131, Reno, NV, 1998.
33. D. V. Gaitone, and M. R. Visbal, *Further Development of a Navier–Stokes Solution Procedure Based on Higher-Order Formulas*, AIAA Paper 99-0557, Reno, NV, 1999.
34. M. Vinokur, An analysis of finite-difference and finite-volume formulations of conservation laws, *J. Comput. Phys.* **81**, 1 (1989).
35. R. Abgrall, Extension of Roe's approximate Riemann solver to equilibrium and nonequilibrium flows, *Notes Numer. Fluid Mech.* **29**, 1 (1990).
36. R. Spekreijse and R. Hagmeijer, Derivation of a Roe scheme for an N-species chemically reacting gas in thermal equilibrium, *Notes Numer. Fluid Mech.* **29**, 522 (1989).
37. F. Chalot, T. J. R. Hughes, and F. Shakib, Symmetrization of conservation laws with entropy for high-temperature hypersonic computations, *Comput. Systems Eng.* **1**, 465 (1990).
38. P. L. Roe, Approximate Riemann solvers, parameter vectors, and difference schemes, *J. Comput. Phys.* **43**, 357 (1981).
39. M. H. Carpenter, D. Gottlieb, S. Abarbanel, and W.-S. Don, The theoretical accuracy of Runge–Kutta time discretizations for initial value problem: A study of the boundary error, *SIAM J. Sci. Comput.* **16**, 1241 (1995).
40. A. Harten and J. M. Hyman, A self-adjusting grid for the computation of weak solutions of hyperbolic conservation laws, *J. Comput. Phys.* **50**, 235 (1983).
41. N. D. Sandham and W. C. Reynolds, *A Numerical Investigation of the the Compressible Mixing Layer*, Report TF-45, Department of Mechanical Engineering, Stanford University, 1989.

42. T. Lumpp, Compressible mixing layer computations with high-order ENO schemes, in *15th Intl. Conf. on Num. Meth. in Fluid Dynamics, Monterey, June 1996.*

43. D. Fu and Y. Ma, A high order accurate difference scheme for complex flow fields, *J. Comput. Phys.* **134**, 1 (1997).

44. N. D. Sandham and H. C. Yee, *Performance of Low Dissipative High Order TVD Schemes for Shock-Turbulence Interactions*, RIACS Technical Report 98.10, NASA Ames Research Center, April 1998.

45. N. D. Sandham and H. C. Yee, *A Numerical Study of a Class of TVD Schemes for Compressible Mixing Layers*, NASA TM-102194, May 1989.

46. H. C. Yee, N. D. Sandham, B. Sjogreen, and A. Hadjadj, *Progress in the Development of a Class of Efficient Low Dissipative High Order Shock-Capturing Methods*, RIACS Technical Report, NASA Ames Research Center, 2000; Proceedings of the Symposium on CFD for the 21st Century, July 15–17, 2000, Kyoto, Japan.